IOP Publishing Plasma Sources Science and Technology
Plasma Sources Sci. Technol. **28** (2019) 095021 (19pp) https://doi.org/10.1088/1361-6595/ab3c7c

Control of charged particle dynamics in capacitively coupled plasmas driven by tailored voltage waveforms in mixtures of Ar and CF_4

S Brandt[1], B Berger[2], Z Donkó[3], A Derzsi[1,3], E Schüngel[4], M Koepke[1] and J Schulze[1,2]

[1] Department of Physics, West Virginia University, Morgantown, West Virginia 26506-6315, United States of America
[2] Institute for Electrical Engineering and Plasma Technology, Ruhr-University Bochum, D-44780 Bochum, Germany
[3] Institute for Solid State Physics and Optics, Wigner Research Centre for Physics, Hungarian Academy of Sciences, 1121 Budapest, Hungary
[4] Evatec AG, Trübbach, Switzerland

E-mail: sbrandt1@mix.wvu.edu

Received 25 March 2019, revised 26 July 2019
Accepted for publication 19 August 2019
Published 24 September 2019

Abstract

The charged-particle power absorption dynamics in capacitively coupled plasmas operated in different CF_4-Ar gas mixtures and driven by tailored voltage waveforms is experimentally investigated by phase-resolved optical emission spectroscopy in conjunction with kinetic simulations and an analytical model. Single- and triple-frequency 'peaks'- and 'valleys'-type waveforms (generated as a superposition of multiple consecutive harmonics of 13.56 MHz) are studied at pressures of 20 and 60 Pa with 25 mm electrode gap and 150 V total driving voltage amplitude to determine the effects of the tailored driving voltage waveform in different gas mixtures on the density profiles of the particle species, the electronegativity, the DC self-bias, and the excitation/ionization dynamics. As the argon content in the buffer gas is increased, the discharge switches from the drift-ambipolar (DA) power absorption mode to the α-mode. This transition occurs due to the disappearance of the bulk and ambipolar electric fields as the electronegativity of the plasma decreases with increasing argon content. This effect is more pronounced at higher pressures, where the negative ion density is higher. We observe a significant change in the plasma's symmetry, DC self-bias, and mean electron energy as a result of the DA- to α-mode transition. At 60 Pa the simulation reveals a drastic increase of the spatially averaged electronegativity induced by increasing the argon admixture from 20% to 30%. This counterintuitive finding is explained by the effect of this admixture on the spatio-temporal electron dynamics. Finally, the generation of the DC self-bias as a function of the argon content is understood by the analytical model based on these fundamental insights into the plasma physics.

Keywords: voltage waveform tailoring, multi-frequency capacitive discharges, electronegative plasmas, electrical asymmetry effect

1. Introduction

Technological plasmas, such as those used in plasma-enhanced chemical vapor deposition [1], reactive sputter deposition [2], the etching of semi-conductors [3, 4], or plasma medicine applications [5–7], frequently require customized local plasma parameters such as the ion flux, the particle energy distribution function, and the plasma

chemistry at a substrate surface for a complicated gas mixture. Optimized process control in such applications necessitates specific flux-energy distributions for electrons, ions and neutrals, which traditionally is not possible in a conventional single-frequency capacitively coupled plasma (CCP) or an inductively coupled plasma (ICP) [8–14]. The charged particle distributions can be manipulated by controlling the spatio-temporal distribution of the electric field in the sheaths adjacent to the surfaces and in the plasma bulk. Limited control is possible for conventional dual frequency discharges operated at significantly different frequencies [14–19] but only in a limited range of operating conditions. Radio-frequency (RF) substrate biasing also allows ICPs to change the average ion energy in a controlled way [20, 21].

A highly promising way to achieve an advanced control of distribution functions is driving RF plasmas with *tailored voltage waveforms* [20, 22–64]. The voltage waveform tailoring (VWT) technique allows for customization of each sheath voltage waveform as well as the time-dependence of the electric field in each sheath and in the plasma bulk on a nano-second timescale. The ion and electron power absorption dynamics, as well as the distribution functions of different particle species, can be controlled as a result [20, 22–26, 29–39, 42–44, 56–60]. Such voltage waveforms can be generated as a superposition of multiple harmonics of a fundamental driving frequency and can be tailored by individually adjusting each harmonic's voltage amplitude and phase. The possible driving waveforms are limited only by the number of applied harmonics. Effective impedance matching of such waveforms is possible with a novel RF supply and matching system [52–54].

Investigations of the effects of the driving voltage waveform on the electron power absorption dynamics [31–38, 44, 56, 60, 65–69] are crucial to gain a fundamental understanding of how such plasmas are generated. These effects are the underlying basis for customizing electron and ion distribution functions, and therefore, process optimization based upon plasma science. One major stride towards this objective was the discovery of the electrical asymmetry effect (EAE) in a CCP driven by two consecutive harmonics by Heil *et al* [23, 70]. Under such an excitation, a DC self-bias is generated as a function of the phase between the driving harmonics. The excitation waveform discussed in [23] generates an asymmetry due to the differing magnitudes of the maximum and minimum applied voltages, which was later referred to as the amplitude asymmetry effect (AAE). The performance of the EAE was verified by simulations [24, 26, 28–30, 46] and experiments [25–30, 45, 51] and was seen to be enhanced by the usage of more than two harmonics [20, 31–39, 42–44, 52, 55]. Another method of generating a discharge asymmetry by driving the plasma with a waveform that has same magnitude of the voltage maximum and minimum, but different 'rising' and 'falling' slopes, i.e. 'sawtooth'-type waveforms, has been proposed by Bruneau *et al* [61–64]. These investigations were primarily limited to electropositive gases operated in the α-heating mode, but more recent works [56–60] have examined electronegative gases operated in the dift-ambipolar (DA-) mode as well [45, 60, 71–76]. VWT is also now being applied to the operation of micro-atmospheric pressure plasmas [77, 78]. A complete fundamental understanding of the effects of VWT on the plasma for arbitrary discharge conditions (discharge geometry, gas pressure, gas admixture, chosen applied voltage waveform, power absorption mode) has not yet been achieved, but is highly incentivized by the desire for finely tuned plasma parameters and the use of complicated gas admixtures in industrial applications [79–83]. For many applications complex gas mixtures are used that contain different admixtures of reactive and/or electronegative gases. Most previous investigations of VWT in CCPs are restricted to a single gas that is either electropositive or -negative. The choice of the gas was found to drastically affect the spatio-temporal dynamics of energetic electrons and the control of process relevant flux-energy distribution functions [22, 46, 56, 64]. Fischer *et al* [60] have, e.g. recently demonstrated that admixing electronegative SF_6 to a CCP driven by tailored voltage waveforms and operated in O_2 drastically affects the DC self bias. This observation was explained by an electron heating mode transition induced by adding more electronegative gas to the plasmas. The spatio-temporal electron dynamics were, however, not studied explicitly in that work. The influence of a chosen gas mixing ratio on discharge operation and process control is strongly correlated to the specific spatio-temporal dynamics dictated by the electron power absorption modes occurring in the plasma. The exact power absorption modes present in a discharge depend on the operating pressure, the characteristics of the driving voltage waveform [20, 31–39, 42–44, 46, 61–69, 71–75, 84–99], and the mixing ratio between gas components [57–59, 100–103]. Therefore, in this work we present a systematic investigation of the electron power absorption dynamics and the EAE in CCPs driven by tailored voltage waveforms at different pressures as a function of the Ar-to-CF_4 gas mixing ratio, which determines the discharge electronegativity. Gas mixtures containing these two gases (electropositive Ar and electronegative CF_4) are frequently used for applications ranging from plasma etching to deposition [79–83]. This study is performed based on a synergistic combination of experiments, particle-in-cell simulations with Monte Carlo treatment of collision processes (PIC/MCC), and modeling. It is highly relevant for such applications, since we investigate the effects of VWT on an industrially relevant scenario and, thus, it allows to assess the potential of this technology for advanced process control. It is also important for fundamental research, since it provides detailed information on the effects of an electropositive gas admixture on an electronegative plasma driven by VWT by revealing its consequences on the spatio-temporal electron dynamics and the DC self bias in detail for the first time. Moreover, it provides an experimental verification of PIC/MCC simulations performed based on this reactive and

electronegative gas mixture. Finally, it reveals a counter-intuitive behavior of the global electronegativity of the plasma as a function of the argon admixture to CF_4. The global electronegativity (β) of the discharge is defined using the ratio of the total number of negative ions to electrons:

$$\beta = \frac{\int_0^d n_i^- \mathrm{d}x}{\int_0^d n_e \mathrm{d}x}, \tag{1}$$

where n_i^- is the negative ion density, n_e is the electron density, and x is the position between the powered (at $x = 0$) and grounded (at $x = d$) electrodes. At a neutral gas pressure of 60 Pa, β is found to increase due to an increase of the argon admixture from 20% to 30%. This finding is explained by the effect of this admixture on the spatio-temporal electron dynamics. The experimental DC self-bias and phase-resolved optical emission spectroscopy (PROES) measurements are compared systematically with results of PIC/MCC simulations to obtain a more complete understanding of the spatio-temporal plasma dynamics across the full range of Ar-to-CF_4 gas mixtures. A voltage balance model [26] is used in conjunction with simulations to analyze the effects of a changing gas mixing ratio on the DC self-bias at different pressures (20 and 60 Pa). The model allows for distinction between different mechanisms causing the generation of the DC self-bias by closely examining the discharge symmetry and the voltage drops across the electrode sheaths and the bulk plasma.

This publication is structured in the following way: in section 2, the experimental setup and all diagnostic methods are introduced. The details of the PIC/MCC code used in the numerical simulations are discussed in section 3. The voltage balance model used for the analysis of the DC self-bias and the discharge symmetry is discussed in section 4. The results are presented in two parts in section 5. First, the spatio-temporal plasma dynamics is examined as a function of the gas pressure and the variation of the argon content in the buffer gas in section 5.1 for triple-frequency 'peaks'-type voltage waveforms in order to provide a fundamental understanding of the plasma physics in CCPs operated in Ar/CF_4 mixtures using tailored voltage waveforms The spatio-temporal distribution of the excitation rate, attachment rate, bulk electric field, mean electron energy, and the time-averaged densities of charged particle species in the plasma are analyzed at each pressure to understand the behavior of the power absorption mode transition from DA- to α-mode as a function of increasing argon content. The effects of the changing spatio-temporal plasma dynamics are then correlated to the changes observed in the generation of a DC self-bias via the EAE in section 5.2, based on the results of the experiments, simulations, and calculations using the model. Finally, the conclusions are given in section 6.

2. Experimental setup

The experimental setup shown in figure 1 consists of a CCP source inside a modified gaseous electronics conference

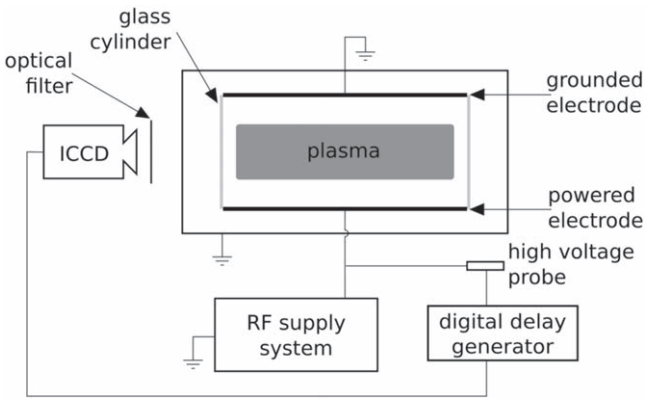

Figure 1. Experimental setup consisting of a capacitively coupled GEC reference cell monitored by diagnostics (PROES via ICCD camera and a high voltage probe).

(GEC) reference cell. The plasma is generated by applying single- and specific multi-frequency voltage waveforms to the powered (bottom) electrode. The other (top) electrode and the chamber walls are grounded. A discussion of the matching network for this setup can be found in [52].

The applied waveform is given by the Fourier series of consecutive harmonics of the fundamental frequency ($f = 13.56$ MHz) [31–38, 44]:

$$\tilde{\phi}(t) = \sum_{k=1}^{N} \phi_k \cos(2\pi k f t + \theta_k), \tag{2}$$

where N is the total number of harmonics, ϕ_k and θ_k are the voltage amplitudes and phases, respectively, of each harmonic (k). The first harmonic's phase is defined as $\theta_1 = 0°$ in equation (2). The total voltage amplitude $\tilde{\phi}_{tot} = \sum_{k=1}^{N} \phi_k$ is fixed at 150 V for all cases and the voltage amplitudes of the individual harmonics are [31]:

$$\phi_k = \tilde{\phi}_{tot} \frac{2(N - k + 1)}{N(N + 1)}. \tag{3}$$

'Peaks'-type waveforms can be generated by setting $\theta_k = 0°$ ($k = 1 \ldots N$), while 'valleys'-type waveforms are obtained by setting the phase angles of the even harmonics to 180°.

The discharge is operated for single-frequency ($N = 1$) and triple-frequency waveforms ($N = 3$, 'peaks'-type and 'valleys'-type waveforms with $\phi_1 = 75$ V, $\phi_2 = 50$ V, and $\phi_3 = 25$ V) for select mixing ratios of CF_4 and Ar gases spanning from pure CF_4 to pure Ar. The electrode gap is fixed at 25 mm between two circular, stainless steel electrodes of 10 cm diameter, and the total gas pressure is set at either 20 or 60 Pa. For each pressure and applied waveform, the mixing ratio of Ar to CF_4 is varied by incrementally increasing the ratio of argon gas flow rate to the total ($Ar + CF_4$) gas flow rate. The total gas flow rate is set to 20 sccm at 20 Pa and 40 sccm at 60 Pa. The relationship between the flow rate and the gas concentrations in the chamber is assumed to be monotonic.

The plasma is radially confined by a glass cylinder, but a geometric asymmetry is present in the discharge due to

capacitive coupling between the glass cylinder and the grounded chamber walls which effectively increases the grounded electrode area. A negative DC self-bias is thus present in the experiments even for single-frequency waveforms.

Two diagnostics are utilized to investigate the discharge: a high voltage (HV) probe used to measure the DC self-bias and an ICCD camera used for PROES. The HV probe requires a calibration between the measurement point on the transmission line and the powered electrode surface [25, 52]. The applied voltage waveform is synthesized by tuning the Fourier amplitudes and phases observed by the HV probe [56].

PROES measurements are performed with high spatial (1 mm) and temporal (2 ns) resolution within the RF period in order to probe the spatio-temporal excitation dynamics of highly energetic electrons responsible for sustainment of the discharge [56, 74, 87, 104–107]. A nano-second gated, high repitition rate ICCD camera (Andor IStar) with an optical filter is synchronized with the applied voltage waveform through a digital delay generator, shown in figure 1, and measures emission from a specifically chosen Flourine atomic transition (F $2s^2 2p^4 3p^1 \rightarrow 3s^1$) at 703.7 nm with a lifetime of 26.3 ns [108]. The optical filter has a central wavelength of 700 nm and a full-width half-maximum of 25 nm. A collisional-radiative model [104] is then used to calculate the spatio-temporal excitation rate between the electrodes and over the RF period. The measured excitation dynamics are indicative of electrons with energies above the excitation threshold of the above level of 14.5 eV. As this line cannot be used in the 100% argon content case, these measurements are executed for argon content values between 0% and 90%. A complete description of this non-invasive optical diagnostic is given in [104].

3. Simulations

Numerical studies of the plasmas created in Ar/CF_4 mixtures are performed with a 1d3v PIC/MCC [109–113]. The electrodes are assumed to be planar and parallel separated by a 25 mm electrode gap. The aspect ratio of the experimental arrangement justifies neglecting the radial losses. The discharge is assumed to be perfectly geometrically symmetric in the simulations. The (bottom) powered electrode is driven by the voltage waveforms specified in section 2, while the other (top) electrode is grounded.

The charged particle species accounted for in the model are CF_3^+, CF_3^-, F^-, and Ar^+ ions, and electrons (e^-). The cross-sections of electron-CF_4/Ar collision processes are the same as those used in previous works [56, 57, 112, 113], which adopted electron-CF_4 processes from Kurihara *et al* [114] except for electron attachment processes (producing CF_3^- and F^- ions) which are adopted from Bonham [115]. Cross-sections for electron-Ar and Ar^+-Ar collision processes are taken from Phelps [116, 117]. The simulations include ion-molecule reactions between CF_3^+, CF_3^-, F^- and CF_4 molecules, as well as elastic scattering of these ions from Ar atoms and elastic scattering of Ar^+ ions from CF_4 molecules [113, 118, 119]. $Ar^+ + Ar$ collisions have a contribution with isotropic scattering and a contribution with backward scattering (charge transfer) [113, 118, 119]. Langevin type cross-sections are employed for elastic collisions between ions and buffer gas molecules/atoms [113, 118, 119]. Ion-ion recombination rates are set at 10^{-13} $m^{-3}\,s^{-1}$ [120, 121]. The electron-CF_3^+ recombination rate is taken from [122]. The electron-induced processes which generate radicals or charged species other than CF_3^+, CF_3^-, F^-, and Ar^+ are included so that they affect the electron kinetics, but the products of these processes are not accounted for. A full list of collision processes included in the simulation can be found elsewhere [56].

We assume a neutral gas temperature of $T = 350$ K in the simulations and include both the emission of secondary electrons due to ion impact and electron reflection at the electrode surfaces. The probability of electron reflection is fixed at 0.2 [123], while the ion induced secondary electron emission coefficient is set at $\gamma = 0.4$. The choice of this relatively large value is justified by the fact that in the experiment, the electrodes are exposed to a relatively high pressure, reactive plasma, where a thin fluorocarbon film with unknown properties is deposited on the electrodes. Moreover, this secondary electron emission yield corresponds to an effective value that includes secondary electron emission processes due to incident particle species other than ions (e.g. photons) as well.

For a given driving voltage waveform, a DC self-bias is generated to equalize the time-averaged electron and positive-ion fluxes to each of the electrodes. The DC self-bias is adjusted in the simulation in an iterative manner to satisfy this particle flux balance [24].

The electron-impact excitation rate from ground state F atoms to the excited state responsible for the 703.7 nm emission measured experimentally by PROES is approximated in the simulations by using the cross-section for an electronic excitation process for CF_4 having an energy threshold of 7.54 eV but accumulating excitation data only for electrons having an energy higher than 14.5 eV, as in a previous work [56]. This calculation is used exclusively for diagnostic purposes and does not affect the total electronic excitation calculated in the simulation and allows us to compare the spatio-temporal excitation dynamics of electrons in the simulation to the experimental PROES measurements without requiring us to explicitly include F atoms in the simulation.

In order to ensure convergence of the simulation the superparticle number of each charged particle species traced in the simulation (electrons, CF_3^+, CF_3^-, F^-) is monitored as a function of time. Convergence is considered to be achieved, when the drift of any of these numbers becomes less than the statistical fluctuation of these quantities (which is at the few % level). We note that convergence is reached on time scales that are significantly longer than those corresponding to electropositive discharges. While in the latter case typically a few thousand RF cycles are known to be sufficient for

convergence, in the CF_4-Ar mixtures studied here, up to 150,000 cycles are simulated before data collection starts. After convergence the data are averaged over 2400 consecutive RF periods to obtain the results shown in the manuscript. In this way highly reliable data are obtained in the same way as in previous simulations performed in pure CF_4. These data have shown excellent agreement with experiments [56].

4. Model and DC self-bias analysis

An analytical model of CCPs and the EAE discovered by Heil *et al* [23] is given in [26]. The DC self-bias, η, is obtained in the model based on the individual voltage drops across the sheaths adjacent to each electrode and across the bulk [23, 26]:

$$\eta = -\frac{\widetilde{\phi}_{\max} + \varepsilon\widetilde{\phi}_{\min}}{1+\varepsilon} + \frac{\phi_{sp}^{f} + \varepsilon\phi_{sg}^{f}}{1+\varepsilon} + \frac{\phi_{\max}^{b} + \varepsilon\phi_{\min}^{b}}{1+\varepsilon} = \eta_{vw} + \eta_{f} + \eta_{b}, \quad (4)$$

where $\widetilde{\phi}_{\max\,/\,\min}$ are the global maximum and minimum of the applied voltage waveform, ϕ_{sp}^{f} and ϕ_{sg}^{f} are the floating potentials at the powered and grounded electrodes, and $\phi_{\max\,/\,\min}^{b}$ are the voltage drops across the bulk at the times of maximum and minimum applied voltage, respectively. The DC self-bias terms have different origins: η_{vw} is due to the applied voltage waveform, η_f is due to the floating potentials at each electrode, and η_b is due to the voltage drop across the bulk plasma. The floating potentials are traditionally considered to be negligible when compared to the applied voltage waveform, such that the η_f term is neglected. The bulk voltage drops in equation (4) can usually be neglected for electropositive plasmas (e.g. argon) at low pressures [124], but cannot generally be ignored if an electronegative gas (e.g. CF_4) is present, as a significant drift electric field often exists in the bulk and a strong ambipolar field can be generated near the sheath edges [45, 46, 65, 71–73, 84, 85, 125]. The existence and strength of these electric field components as a function of the mixing ratio between the electronegative and electropositive component gases at a given pressure is not well understood at present. The term from the applied voltage waveform, η_{vw}, in equation (4) is typically dominant compared to the other terms, even in electronegative plasmas. The global extrema of the driving voltage waveform, $|\widetilde{\phi}_{\max}|$ and $|\widetilde{\phi}_{\min}|$, can be made unequal by applying two or more consecutive harmonics of a fundamental frequency with distinct relative phases. The effect of inducing a difference between the driving voltage waveform's global extrema on the η_{vw} self-bias term, via $\widetilde{\phi}_{\max\,/\,\min}$, is known as the AAE.

The symmetry parameter in equation (4) is defined as:

$$\varepsilon = \frac{|\hat{\phi}_{sg}|}{|\hat{\phi}_{sp}|} \approx \left(\frac{A_p}{A_g}\right)^2 \frac{\bar{n}_{sp}}{\bar{n}_{sg}} \left(\frac{Q_{mg}}{Q_{mp}}\right)^2 \frac{I_{sg}}{I_{sp}}, \quad (5)$$

where $|\hat{\phi}_{sp}|$ and $|\hat{\phi}_{sg}|$ are the maximum voltage drops across each sheath (note that $\hat{\phi}_{sp} < 0$ V and $\hat{\phi}_{sg} > 0$ V) [26]. The terms on the right hand side of equation (5) correspond to the ratios of the respective electrode surface areas, A_p and A_g, the respective mean net charged particle densities in each sheath, $\bar{n}_{sp}$ and $\bar{n}_{sg}$, the maximum uncompensated charges in each sheath, Q_{mp} and Q_{mg}, and the sheath integrals for each sheath, I_{sp} and I_{sg}, as discussed in [23, 26, 124, 126]. The symmetry parameter's dependence on the charge densities in each sheath suggests a dependence on the electron power-absorption mode through the localization of ionization, which is the basis for the slope asymmetry effect (SAE) [61–64]. This becomes particularly relevant in electronegative discharges at high pressures where the DA-mode is dominant, as the electron power absorption is primarily located at the collapsing sheath edge and in the bulk plasma in contrast with the α-mode, where maximum ionization is observed at the expanding sheath [56, 57].

In geometrically symmetric CCPs, the DC self-bias can thus be controlled using two mechanisms that aim to modify the η_{vw} self-bias term: $|\widetilde{\phi}_{\max}| \neq |\widetilde{\phi}_{\min}|$ (AAE) or $\varepsilon \neq 1$. One way to cause the symmetry parameter to deviate from unity is the use of the SAE, which can be induced by using sawtooth waveforms

The 'peaks'-voltage waveform cases for $N = 3$ are examined for both 20 and 60 Pa by using the simulation results as inputs to the above model. The sheath potentials ($\phi_{sp}(t)$, $\phi_{sg}(t)$), the applied voltage waveform ($\tilde{\phi}(t)$), the DC self-bias (η), the symmetry parameter (ε), the floating potentials at each electrode (ϕ_{sp}^{f}, ϕ_{sg}^{f}), and the bulk voltage at the times of maximum and minimum applied voltage ($\phi_{\max\,/\,\min}^{b}$) are used as inputs into equations (4) and (5) in order to calculate the DC self-bias, η, based on equation (4). In this way, the contributions of η_{vw}, η_b, and η_f and the different mechanisms of DC self-bias generation can be separated. The evolution of η_b is then correlated to the changes in the global electronegativity (β) from equation (1), which is also extracted from the simulations. The evolution of the symmetry parameter ε from equation (5) with the changing gas mixture is also contextualized in the model by calculating each of its individual ratio components $\left(\frac{Q_{mg}}{Q_{mp}}\right)^2$, $\frac{\bar{n}_{sp}}{\bar{n}_{sg}}$, $\frac{I_{sg}}{I_{sp}}$, with $\left(\frac{A_p}{A_g}\right)^2 = 1$. The time-averaged charged particle density in each sheath, the uncompensated charge in each sheath ($Q_{sp}(t)$, $Q_{sg}(t)$), and the maximum sheath widths (l_{sp}, l_{sg}) from the simulation are used to calculate the symmetry parameter terms Additionally, an example geometric asymmetry is implemented into the model by setting $\frac{A_p}{A_g} = 0.25$ but otherwise keeping the calculations for the symmetry parameter terms the same in order to study the effects of an exemplary geometric reactor asymmetry on the DC self-bias generation qualitatively.

5. Results

As the effects of varying the Ar-to-CF_4 mixing ratio, and thus the plasma's electronegativity, on CCPs driven by tailored voltage waveforms are best understood by first examining the spatio-temporal dependence of the electron impact excitation/

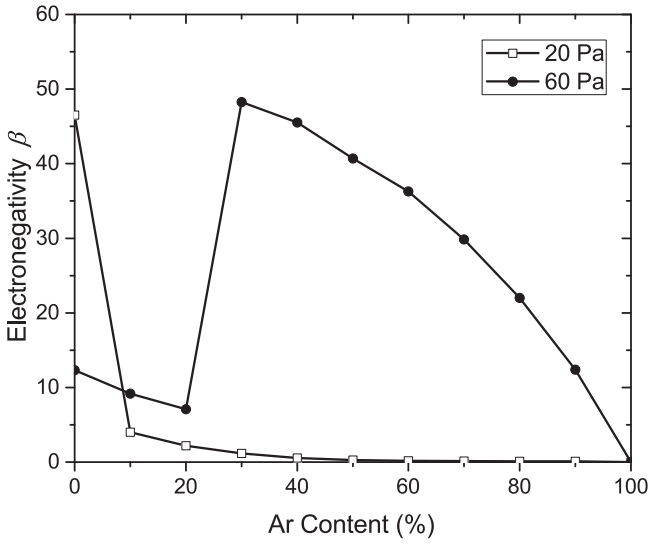

Figure 2. Global electronegativity (β) of the discharge obtained from the PIC/MCC simulation for the 'peaks'-waveform ($N = 3$, $\tilde{\phi}_{\mathrm{tot}} = 150$ V) as a function of the argon content in the buffer gas at 20 Pa (open boxes) and 60 Pa (closed circles).

ionization rate, attachment processes, electric field, and the mean electron energy, we start with discussing the experimental and simulation results for these quantities in section 5.1. These spatio-temporal dynamics and results of the analytical model are then linked to the DC self-bias evolution seen in both the simulations and the experiments in section 5.2.

5.1. Spatio-temporal dynamics in Ar/CF_4 gas mixtures

The global electronegativity (β) obtained from the PIC/MCC simulations is shown as a function of the argon content in the buffer gas for the 'peaks'-waveform at 20 and 60 Pa in figure 2. For 20 Pa, the electronegativity is significant only in the pure CF_4 case and decreases dramatically with increasing argon content, until approximately 30% Ar, where it becomes negligible. This trend represents a typical transition of an electronegative to an electropositive plasma induced by gradually replacing the electronegative by an electropositive gas. At 60 Pa, however, the global electronegativity exhibits a more complex and counterintuitive variation across the 0%–100% argon content interval in the simulations, moving from a low value for 0%–20% Ar to a highly electronegative regime, where β decreases with increasing argon content but remains significant even up to 90% Ar. In fact, adding more electropositive gas is found to increase the global electronegativity for argon admixtures between 20% and 30%. This finding will be explained based on the effects of adding argon on the spatio-temporal electron dynamics. The low values of β in the 0%–20% argon content interval for 60 Pa are attributed to the fact that the plasma is divided into a weakly and a strongly electronegative region under these conditions, while it is strongly electronegative in the whole discharge for 30%–90% Ar (as will be shown in detail below). For instance, in the pure CF_4 plasma, the local electronegativity is approximately 8 and 62 on the bulk side of the sheath edge at the powered and grounded electrode, respectively. The presence of the weakly electronegative region for 0%–30% Ar reduces the global electronegativity. The physical origin of the strongly electronegative region adjacent to the grounded electrode at low Ar admixtures at 60 Pa is the formation of a potential well at the grounded electrode, which confines negative ions. This, in turn, is caused by the specific shape of the driving voltage waveform, which causes the sheath at the grounded electrode to be collapsed for most of the fundamental RF period and local maxima of the electron density at the position of the maximum sheath width. At the grounded electrode this leads to the formation of an ambipolar field that accelerates negatively charged particles towards this electrode. A potential well is caused by this ambipolar field and the floating potential at the electrode. The presence of the ambipolar electric field causes significant electron power absorption and, thus, a high mean electron energy at the time of high RF current, when the local sheath collapses. This enhances the attachment, whose cross section has a narrow peak within an electron energy interval of 5–10 eV, and, thus, the local negative ion density, which self-amplifies this effect. This phenomenon is discussed in detail in reference [56] for a pure CF_4 discharge.

The spatio-temporal electron impact excitation rate for the 703.7 nm fluorine line obtained from the PIC/MCC simulation, which assumes a geometrically symmetric discharge, is shown in figure 3 for the 'peaks'-waveform at both 20 Pa (figures 3(a)–(c)) and 60 Pa (figures 3(d)–(f)) for the 0% Ar, 50% Ar, and 90% Ar cases. The sheath edges are computed using the Brinkmann criterion [127] taking the presence of negative ions into account and are shown as white lines in each plot. The maximum absolute value of the excitation rate is observed to decrease both as the argon content is increased and as the pressure is decreased. In general, there are two separate mechanisms of electron acceleration that cause excitation maxima at different positions and times within the fundamental RF period: (i) α-mode excitation is caused by electron power absorption on the bulk side of the expanding sheath edge. (ii) DA-mode excitation maxima occur on the bulk side of the collapsing sheath edge and are caused by the local maxima of the electron density at the position of the maximum sheath width in electronegative CCPs. These cause ambipolar electric fields that accelerate electrons towards the adjacent electrode. Here, a transition from the DA power absorption mode to a hybrid DA-/α-mode is observed at both pressures as a function of increasing argon content. At 60 Pa, the mode transition has a different behavior with increasing argon content where the DA-mode heating is sustained to much higher argon content values. For example, the DA-mode heating remains dominant at 50% Ar (figure 3(e)) and remains relevant even for 90% Ar (figure 3(f)). This confirms the results shown in figure 2, where at 60 Pa the electronegativity (β) is about 40 and 15 for 50% Ar and 90% Ar, respectively. In the 0%–20% Ar range at 60 Pa (e.g. figure 3(d) and in figure 2), a highly localized DA-mode is observed with excitation maxima only at the collapsing sheath of the grounded electrode, similar to that observed in a previous work in pure CF_4 [56]. The change in the localization of

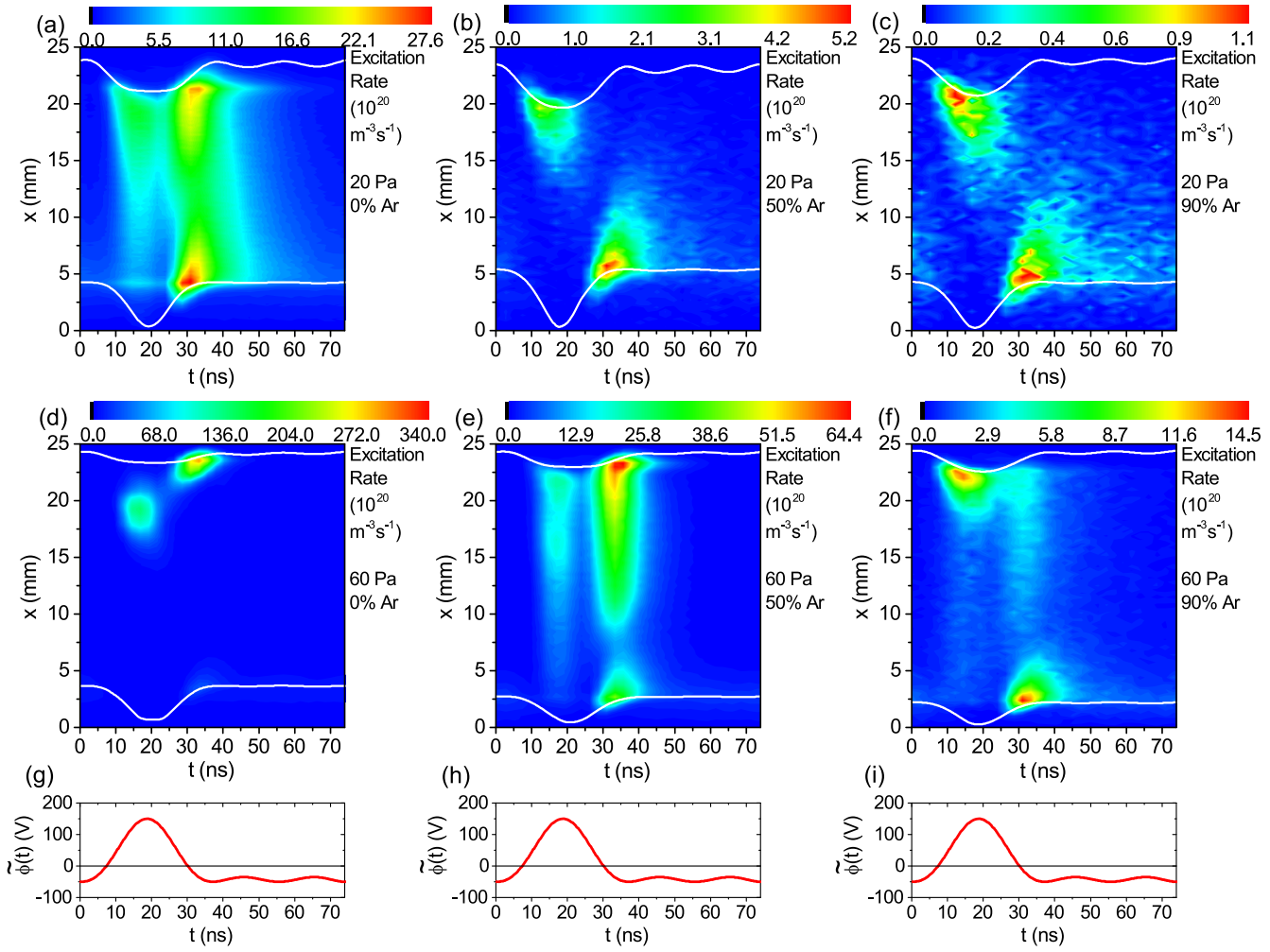

Figure 3. Spatio-temporal distribution of the electron impact excitation rate for the 703.7 nm fluorine line (excitation threshold energy: 14.56 eV) obtained from PIC/MCC simulations for the 'peaks'-waveform ($N = 3$, $\tilde{\phi}_{tot} = 150$ V) at 20 Pa (a)–(c) and 60 Pa (d)–(f), as a function of argon content in the buffer gas. The sheath edges are marked by the white lines based on the Brinkmann criterion [127]. The driving voltage waveform is shown for reference in (g)–(i). The powered electrode is located at $x = 0$ mm, while the grounded electrode is at $x = 25$ mm.

the excitation/ionization in figures 3(d)–(f) from near the grounded sheath (DA-mode) to near the powered sheath (α-mode) is quite significant at 60Pa in the simulations. It is thus easily conceivable that the symmetry parameter ε, which depends explicitly on the ratio of the ion density in both sheaths, would be dramatically changed by the mode transition with increasing argon content in the 60 Pa case (see later in figure 10(a)). At 20 Pa, a hybrid DA-α mode exists near 0% Ar and the discharge transitions to a pure α-mode near 30% Ar, in contrast to the DA-mode being sustained to almost 90% Ar for 60 Pa. The reduced change in excitation localization for 20 Pa implies that the symmetry parameter ε is expected to vary little with increasing argon content as a result (see later in figure 10(a)). The different behavior of the mode transition with increasing argon content at 20 and 60 Pa is caused by the different electronegativity (see figure 2).

Figure 4 shows the results of the PROES measurements at 20 Pa (panels (a)–(c)) and 60 Pa (panels (d)–(f)) for the 'peaks'-waveform for 0%, 50%, and 90% argon content. Compared to the results of the simulations, performed for the same discharge conditions (see figure 3) and considering the complex chemistry as well as the geometric reactor asymmetry in the experiment, reasonable qualitative agreement between experimental and computational results is found. The differences in figures 3 and 4 are caused by the presence of a geometric asymmetry in the experiment, which is not included in the PIC/MCC simulations. In contrast to figure 3, the α-mode excitation near the powered electrode is significantly stronger than that at the grounded electrode even in the 60 Pa, 0% Ar case. This is caused by the presence a more negative DC self-bias in the experiment due to the geometric discharge asymmetry. This results in a smaller change in the localization of the excitation/ionization across the discharge in the experiment as the argon content is increased, in turn suggesting that any ε variation is also smaller in the experiment. The sustainment of the DA-mode to very high argon content values at 60 Pa seen in figures 3(d)–(f) is confirmed by the experimentally measured excitation rates in figures 4(d)–(f). Similarly, at 20 Pa, the DA-α mode transition occurs at a smaller argon content value than that at 60 Pa, and the weaker

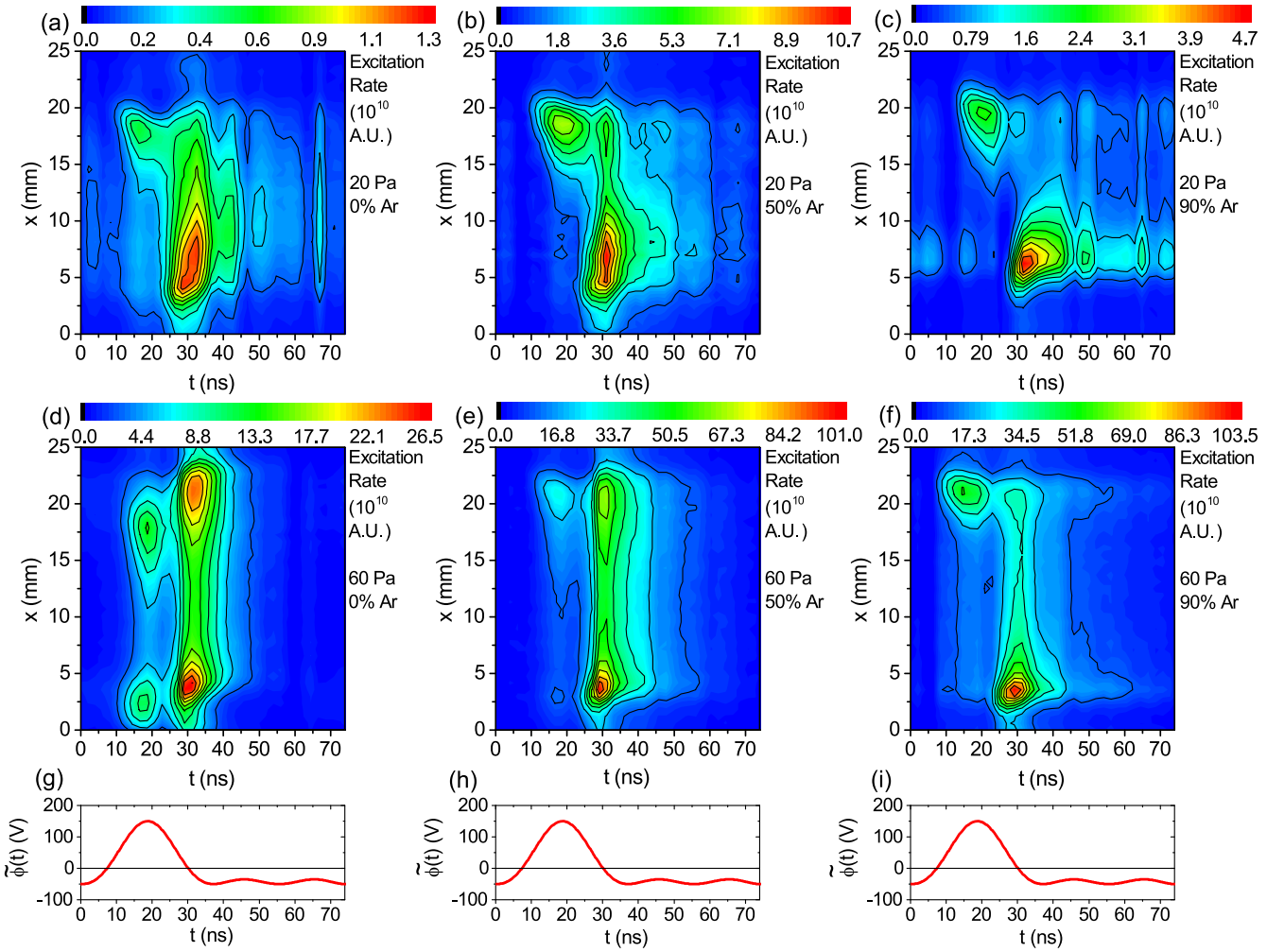

Figure 4. Spatio-temporal distributions of the electron impact excitation rate of the 703.7 nm fluorine line obtained via PROES in the experiment for the 'peaks'-waveform ($N = 3$, $\tilde{\phi}_{tot} = 150$ V) at 20 Pa (a)–(c) and 60 Pa (d)–(f), as a function of argon content in the buffer gas. The driving voltage waveform is shown for reference in (g)–(i). The powered electrode is located at $x = 0$ mm, while the grounded electrode is at $x = 25$ mm.

mode transition should not significantly change the plasma symmetry.

The DA power absorption of electrons in the plasma bulk is caused by a significant density of negative ions in the bulk plasma and, thus, a depleted electron density. This leads to a reduced conductivity in the bulk and the generation of an enhanced bulk electric field required to drive the current. Consequently, electrons are accelerated to high energies in the bulk and cause excitation at the times of high current. Negative ion formation proceeds via collisional attachment processes, whose cross-sections are high only within an energy interval of 5–10 eV for CF_4 [114, 115]. The total attachment rate obtained from the simulation is shown for the 'peaks'-waveform at 20 and 60 Pa for 0%, 50% and 90% argon content in figure 5. At 20 Pa (figures 5(a)–(c)), this rate is comparably much lower than for the 60 Pa cases throughout the discharge and becomes insufficient to sustain the DA-mode at a much lower argon content value due to the decreased mean electron energy at that pressure. This leads to a lower negative ion density, a less depleted electron density, lower electronegativity (as in figure 2), and thus a substantially weaker DA-mode for 20 Pa. This also constitutes the well-known phenomenon of the DA-mode being primarily induced at higher pressure in CF_4 [46, 103].

At 60 Pa, an increase of the global electronegativity as a function of the argon admixture for admixtures between 20% and 30% is found (see figure 2). This is accompanied by a change of the spatio-temporal electron dynamics from excitation adjacent to the grounded electrode at 0% argon admixture to excitation throughout most of the plasma bulk at higher admixtures of argon, e.g. 50% (see figure 3(d) and (e)). The simulations reveal that this excitation is caused by electrons accelerated by drift and ambipolar electric fields, which are present only at the position, where excitation is observed (see figures 7(d) and (e)). These findings are explained by the following mechanism: adding a small admixture of argon to an electronegative CF_4 discharge, causes a higher plasma density, since the ionization threshold of argon is lower compared to CF_4. A corresponding increase of the total positive ion density is observed in figures 6(d) and (e), which show, respectively, the time averaged charged particle density profiles for 0% and 50% argon admixtures. Consequently, the

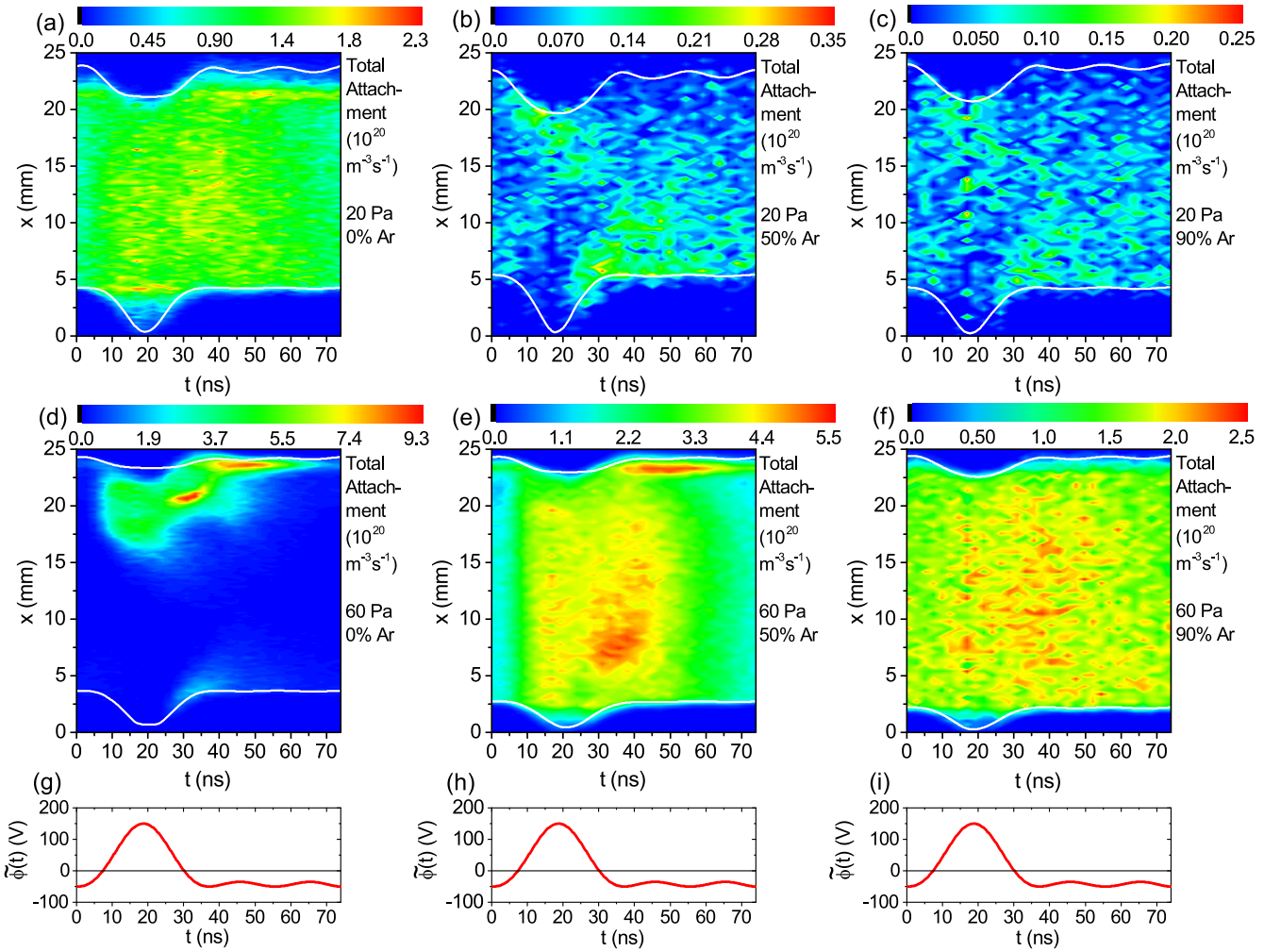

Figure 5. Spatio-temporal distributions of the total attachment rate from the simulation for the 'peaks'-waveform ($N = 3$, $\tilde{\phi}_{\mathrm{tot}} = 150$ V) at 20 Pa (a)–(c) and 60 Pa (d)–(f), as a function of argon content in the buffer gas. The sheath edges are marked by the white lines based on the Brinkmann criterion [127] in each plot. The driving voltage waveform is shown for reference in (g)–(i). The powered electrode is located at $x = 0$ mm, while the grounded electrode is at $x = 25$ mm.

total positive ion fluxes to the electrodes increase as a function of the argon admixture. In order to compensate the positive ion flux to the electrodes, the electron current must also increase at the times of sheath collapse during each fundamental RF period. However, in the presence of a high admixture of CF_4, most electrons are lost via attachment to form negative ions. This leads to a low conductivity and a high electric field at times of high current within each fundamental RF period required to sustain the electron current, which is needed to compensate the ion flux at each electrode on time average. Thus, the few electrons are accelerated to relatively high energies (see figure 8). In this way a positive feedback loop is formed that leads to the generation of a high electronegativity for small argon admixtures, since the cross section for the formation of negative ions via electron attachment in CF_4 is maximum at high electron energies between 5 and 10 eV. This mechanism explains the counter-intuitive finding that the global electronegativity is higher for small argon compared to no argon admixture. It proceeds primarily via an increase of the electronegativity at the powered electrode. For high admixtures of argon the global electronegativity decreases again, since the formation of negative ions is reduced due to the absence of CF_4 molecules as collision partners. As the currents and the electric field are increased as a function of argon admixture (for low admixtures) the dissipated power also increases (not shown). In fact, the dissipated power follows the trend of the global electronegativity as a function of argon admixture shown in figure 2 at 20 and 60 Pa.

The time-averaged densities of each charged particle species traced in the simulation for the 'peaks'-waveform cases are shown in figure 6. For 20 Pa, the negative ion and electron densities (i.e. the local electronegativity) remain spatially uniform in the plasma bulk. On the other hand, at 60 Pa, the discharge is split into two halves of strongly different electronegativity at 0% Ar according to the spatially asymmetric distribution of the attachment rate shown in figure 5(d). The plasma exhibits a spatially nearly uniform but still electronegative density profile near an argon content value of 50%. The electronegativity is still quite significant even for the 90% Ar case at 60 Pa, allowing for the presence

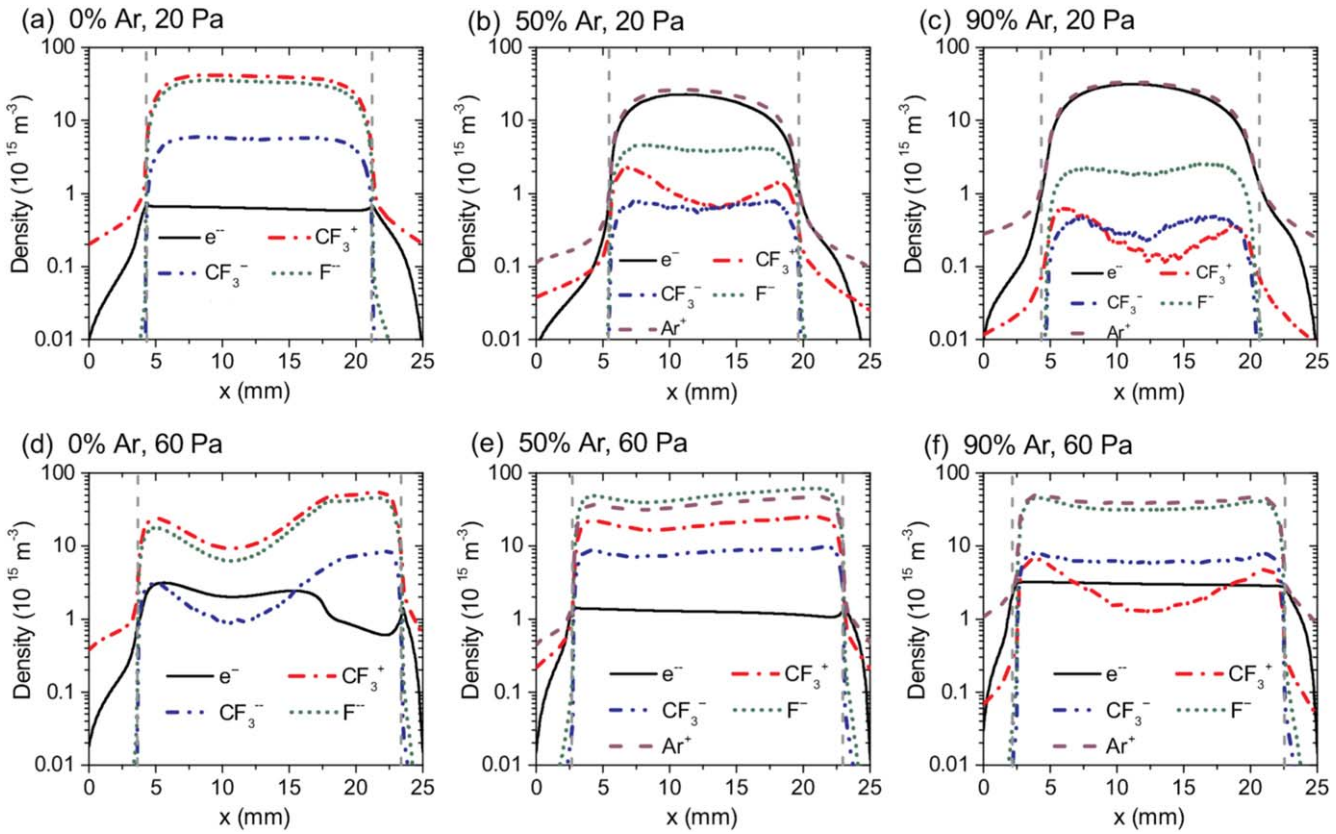

Figure 6. Simulation results for the time-averaged densities of each charged particle species traced in the simulation (CF_3^+, CF_3^-, F^-, Ar^+, and electrons) as a function of position x between the powered ($x = 0$ mm) and grounded ($x = 25$ mm) electrodes for the 'peaks'-waveform ($N = 3$, $\tilde{\phi}_{tot} = 150$ V) at 20 Pa (a)–(c) and 60 Pa (d)–(f), and as a function of argon content in the buffer gas. The maximum sheath widths are marked by the gray dashed vertical lines based on the Brinkmann criterion [127] in each plot.

of significant electric fields and DA-mode heating in the bulk plasma.

Spatio-temporal plots of the electric field determined from the simulation are shown in figure 7 at 20 and 60 Pa for various argon content values. Under conditions of high electronegativity a strong drift field in the bulk and an ambipolar field at the grounded electrode are observed [45, 46, 65, 71–73, 84, 85, 125]. For 20 Pa, this bulk electric field disappears for high argon contents, i.e. above 30% Ar, as the discharge electronegativity and the attachment rate become negligible (figures 2 and 5(b)–(c)). In the 20 Pa, 0% Ar and the 60 Pa cases, though, significant electric fields are observed in the discharge bulk. The localized DA-mode present at low argon content values for 60 Pa is characterized by strong electric field maxima on the bulk side of the sheath edge at the grounded electrode, as shown in figure 7(d). The strength of this localized field is much higher than that of the almost homogeneous field typically observed in DA-mode plasmas [45, 46, 65, 71–73, 84, 85, 125], but it also occurs across a smaller spatial region. As this high local electric field oscillates within the fundamental RF period, it is associated with a significant displacement current. For 0% argon admixture at 60Pa, the electric field is low in the rest of the bulk, since the local electronegativity is low in this region compared to the strongly electronegative region close to the grounded electrode. This leads to a higher conductivity and a lower electric field required to drive the current through the bulk.

Figure 8 shows the spatio-temporal distribution of the mean electron energy for the 'peaks'-waveforms cases. The acceleration of electrons by the DA- or α-power absorption modes allows for efficient attachment at 60 Pa (figures 8(d)–(f)), as the mean electron energy in the bulk plasma is in the 5–10 eV energy range of the CF_4 attachment cross-sections [114, 115] resulting in the high attachment rates seen in figure 5. The DA-mode heating of bulk electrons and the reduction in attachment rate at 60 Pa and 90% argon (see figure 3(f) and figure 5(f)) lead to a small variation in the mean electron energy (4–6 eV) across the RF period (figure 8(f)). The distribution of electrons with energies required for generating reactive radicals may also change dramatically in space with increasing argon content, which could potentially lead to differing flux distributions of these radical species towards each electrode. These radical flux distributions could then potentially be adjusted as a function of the gas mixture for optimizing processes which require specific ion-to-radical flux ratios.

5.2. Effect of gas composition on the DC self-bias

The understanding of the DC self-bias generation is important in applications since η influences both the ion flux-energy

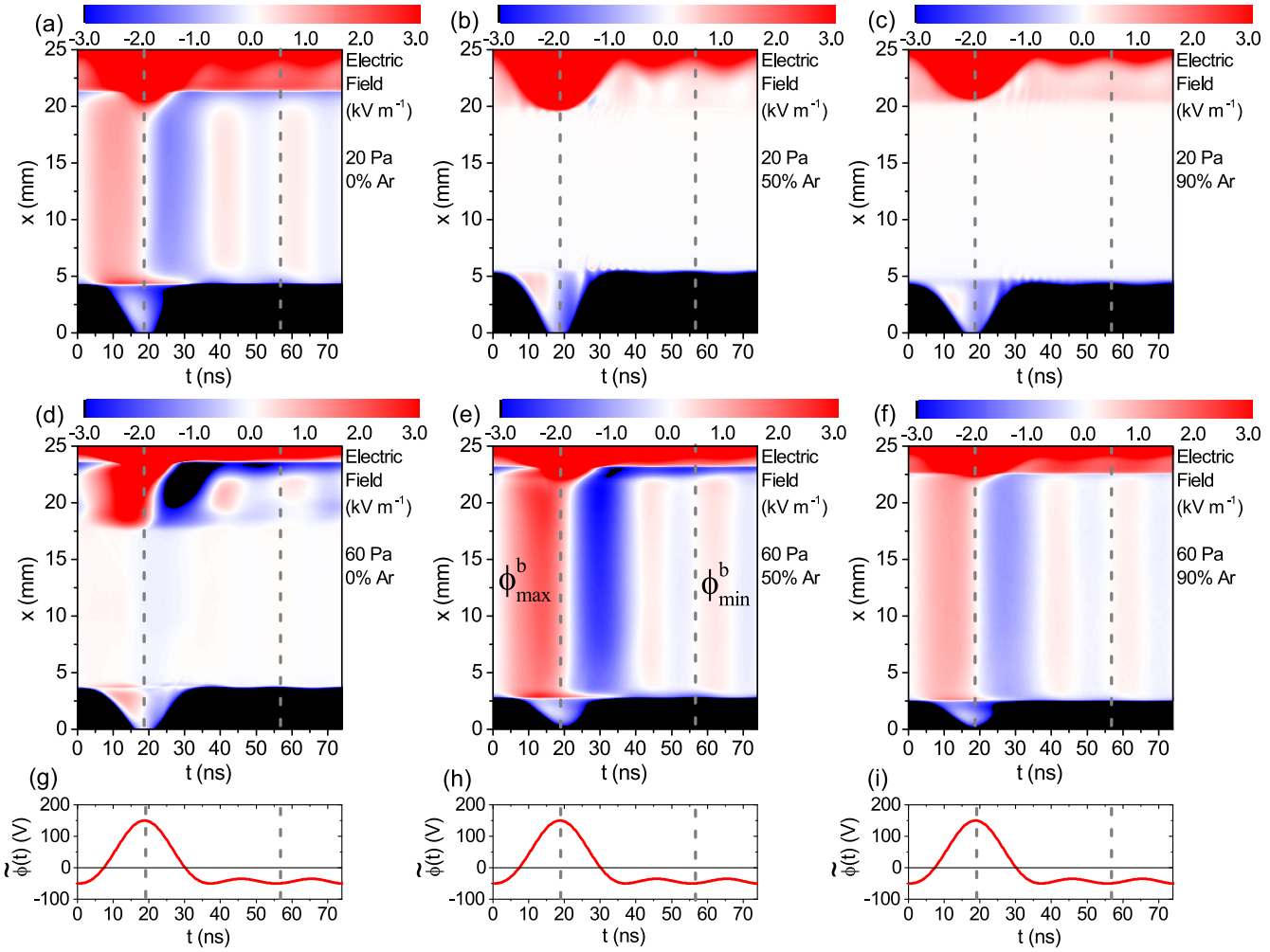

Figure 7. Spatio-temporal distribution of the electric field (kV m^{-1}) obtained from the simulation for the 'peaks'-waveform ($N = 3$, $\tilde{\phi}_{\mathrm{tot}} = 150$ V) at 20 Pa (a)–(c) and 60 Pa (d)–(f), as a function of argon content in the buffer gas. The color scale is chosen in a way to make the electric field in the plasma bulk visible. The driving voltage waveform is shown for reference in (g)–(i). The dashed vertical lines indicate the times of maximum (at ≈19 ns) and minimum voltage (at ≈57 ns) of the driving voltage waveform at which $\phi^{\mathrm{b}}_{\mathrm{max\,/\,min}}$ are calculated. The powered electrode is located at $x = 0$ mm, while the grounded electrode is at $x = 25$ mm.

distribution functions at plasma-facing surfaces and the electron power absorption dynamics. Figure 9 shows the DC self-bias as a function of the argon content in the buffer gas for single-frequency ($N = 1$) and triple-frequency ('peaks' and 'valleys', $N = 3$) waveforms obtained from the experiment and the simulations at 20 and 60 Pa. In the single frequency case, the experiment exhibits a normalized self bias (DC self-bias voltage divided by the total driving voltage amplitude) of approximately −15% at 20 Pa, which is insensitive of the argon content. At 60 Pa, η is zero in a pure CF_4 discharge and its magnitude increases to about 12% at high argon content. The DC self-bias is negative because of the presence of a larger grounded compared to powered electrode surface in the experiment. It is, however, zero in the simulations for $N = 1$ independent of the argon content, since no geometric discharge asymmetry is included and there is no electrical asymmetry.

For the triple frequency 'peaks-/valleys'-waveforms we find significantly different values of the DC self-bias compared to the single frequency case due to the presence of the EAE and the spatio-temporal electron dynamics described in the previous section. At 20 Pa we find good agreement between experimental and simulation results in terms of the dependence of η on the argon content. The only difference is an approximately constant shift caused by the geometric reactor asymmetry, which is only present in the experiment. At 60 Pa some deviations are observed. As will be explained later, these are also caused by the geometric discharge asymmetry in the experiment. For the 'peaks'-waveform the DC self-bias is negative at both pressures, while it is positive for the 'valleys'-waveforms At 20 Pa it is independent of the argon admixtures for both waveforms, while its magnitude decreases as a function of the argon content at 60 Pa in the simulation.

In order to understand the dependence of the DC self-bias on the argon content at 20 and 60 Pa we use the analytical model introduced in section 4. In the frame of this model, the DC self-bias is described by equations (4) and (5). It is

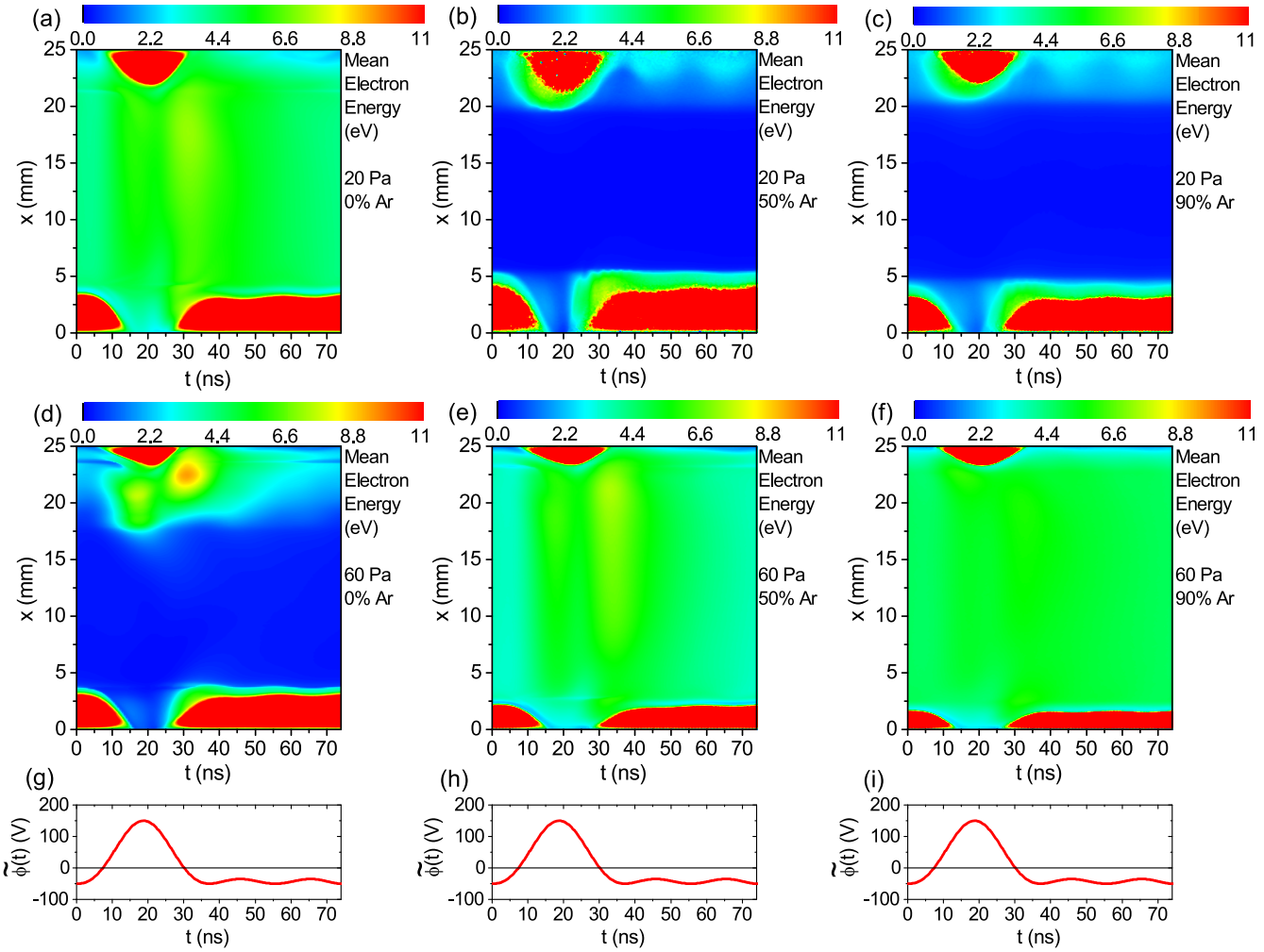

Figure 8. Spatio-temporal distribution of the mean electron energy obtained from the simulation for the 'peaks'-waveform ($N = 3$, $\tilde{\phi}_{\mathrm{tot}} = 150$ V) at 20 Pa (a)–(c) and 60 Pa (d)–(f), as a function of argon content in the buffer gas. The driving voltage waveform is shown for reference in (g)–(i). The powered electrode is located at $x = 0$ mm, while the grounded electrode is at $x = 25$ mm.

determined by the sum of three terms: η_{vw} related to the applied voltage waveform, η_{f} due to the floating potentials at each electrode, and η_{b} resulting from the voltage drop across the bulk plasma. The floating potentials are neglected in our analysis due to their small magnitude.

In both terms, η_{vw} and η_{b}, the symmetry parameter, ε, plays an important role. Therefore, we analyze the behavior of ε obtained from the PIC/MCC simulation as a function of argon content at both pressures for 'peaks'-waveforms (see figure 10(a)). In a geometrically symmetric discharge, which is the case in the simulation, the symmetry parameter is largely determined by the ratio of the mean ion densities in both sheaths. This ratio is, in turn, determined by the spatio-temporal dynamics of energetic electrons via their effects on the ionization probed by the excitation here (see figures 3 and 4). At 20 Pa, the ratio of the maxima of the excitation rate at both electrodes does not change much as a function of the argon content. Thus, ε is independent of the argon content. At 60 Pa, however, by admixing more argon the mode of discharge operation is changed from the DA- to the α-mode. This causes the ratio of the excitation maxima adjacent to both electrodes and the symmetry parameter to change as a function of the argon content as well.

The dependence of ε on the argon content affects the two calculated self-bias terms, η_{vw} and η_{b}, in the model, which are shown in figure 10(b) as a function of the argon content for both 20 and 60 Pa. Recall that, for a fixed applied voltage waveform, $\tilde{\phi}_{\mathrm{max\,/\,min}}$ do not change, such that changes in η_{vw} are solely due to changes in the symmetry parameter (ε) due to the mode transition induced by the decreasing electronegativity with the argon content (figure 2).

The variation of η_{b} is a result of the change in ε and changes of the voltage drops across the plasma bulk at the times of maximum and minimum driving voltage, $\phi^{\mathrm{b}}_{\mathrm{max,min}}$. These voltage drops across the bulk are obtained from the simulations at the times indicated in figure 7. At 60 Pa, the presence of the oscillating drift electric field in the bulk implies a non-zero, time-dependent bulk voltage, $\phi^{\mathrm{b}}(t)$. In the presence of a 'peaks'-driving voltage waveform $|\phi^{\mathrm{b}}_{\mathrm{max}}| > |\phi^{\mathrm{b}}_{\mathrm{min}}|$ under these conditions, because the RF currents are different at these two characteristic times and, thus, different bulk electric fields are required to drive these

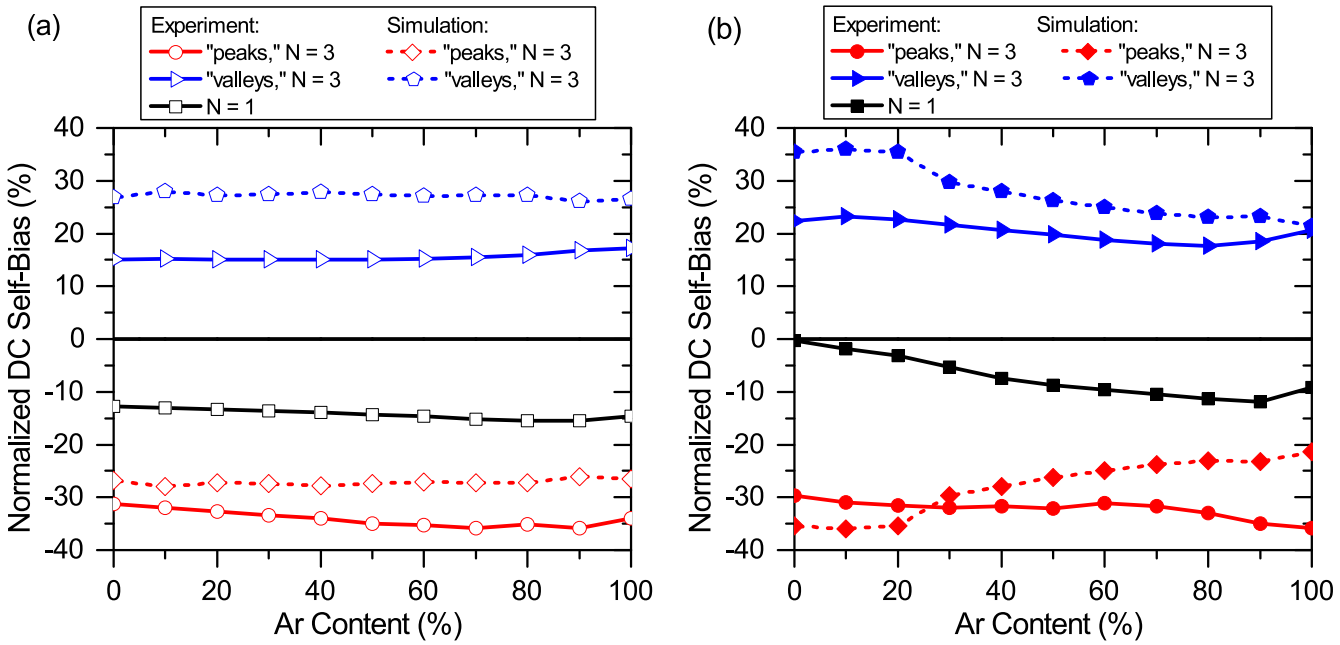

Figure 9. DC self-bias normalized by the total driving voltage amplitude as a function of the argon content in the buffer gas for single-frequency ($N = 1$) and triple-frequency ('peaks' and 'valleys', $N = 3$) waveforms obtained from the experiment and the simulations at 20 Pa (a) and at 60 Pa (b), for a 25 mm electrode gap and $\widetilde{\phi}_{\mathrm{tot}} = 150$ V.

currents. In combination with the change of the symmetry parameter as a function of the argon content this causes $\eta_{\mathrm{b}} > 0$ V at 60 Pa (see equation (4) and figure 10(b)). The voltage drops across the plasma bulk at the times of maximum and minimum applied voltage decrease as a function of argon content, since the discharge gets more electropositive and, thus, the drift electric field in the bulk decreases. At 20 Pa, the drift electric field in the bulk is lower, since the conductivity is higher compared to the 60 Pa case due to a lower electron-neutral collision frequency and a lower electronegativity for most argon admixtures. Moreover, ε is constant as a function of the argon content due to the absence of any strong mode transitions. Thus, η_b is essentially zero under these conditions.

Figure 10(c) shows the DC self-bias as a function of the argon content at 60 Pa obtained from the simulation and the analytical model. In the model, the DC self-bias is calculated as the sum of η_{vw} and η_{b}. Excellent agreement between the simulation and the model results is found. This shows that the floating potential term can indeed be neglected and that the model can be used to understand the generation of the DC self-bias as a function of the argon content under these conditions.

In order to obtain a more detailed understanding of the DC self-bias generation in this reactive electronegative CCP, the evolution of the symmetry parameter, ε, for the 'peaks'-waveform at 60 Pa as a function of the argon content is investigated by calculating each individual term in equation (5) using simulation data as inputs to the model, assuming that the discharge is geometrically symmetric, i.e. $\left(\frac{A_{\mathrm{p}}}{A_{\mathrm{g}}}\right)^2 = 1$. The results of this analysis can be seen in figure 11, where each term's variation with increasing argon content, as well as the ε reconstructed from the model calculations, are shown in figures 11(a) and (b), respectively. The changes in ε with increasing argon content are almost exclusively due to the strong increase in the sheath charged particle density ratio $\frac{\bar{n}_{\mathrm{sp}}}{\bar{n}_{\mathrm{sg}}}$, corresponding to the change in spatial localization of the discharge ionization as a function of the dominant power-absorption mode. The ratio of the maximum uncompensated charges in both sheaths as well as the ratio of the sheath integrals do not change much as a function of the argon content.

The symmetry parameter, ε, is calculated based on the individual terms in equation (5) from figure 11(a) and is compared to the ε directly provided as an output from the simulations in figure 11(b). Good agreement is found between the ε obtained from the model and that obtained from the simulation. The ε from the model is then calculated again, but with an 'artificial' geometric asymmetry set at $\frac{A_{\mathrm{p}}}{A_{\mathrm{g}}} = 0.25$ in equation (5) to demonstrate the effect of a geometric asymmetry on the variation of ε qualitatively. This does not account for the changes in sheath density which would occur in the presence of such a geometric asymmetry, and the specific value of $\frac{A_{\mathrm{p}}}{A_{\mathrm{g}}}$ in the measurements, where a significant geometric asymmetry is present, may not match this example value. The corresponding line in figure 11(b) demonstrates that the changes in ε are strongly damped by the presence of the geometric asymmetry. It is then expected that the variation of the η_{vw} self-bias term as a function of the argon content would similarly be reduced in the presence of a significant geometric asymmetry, leaving η_{b} to be the primary cause of changes in the total DC self-bias η in the experiment.

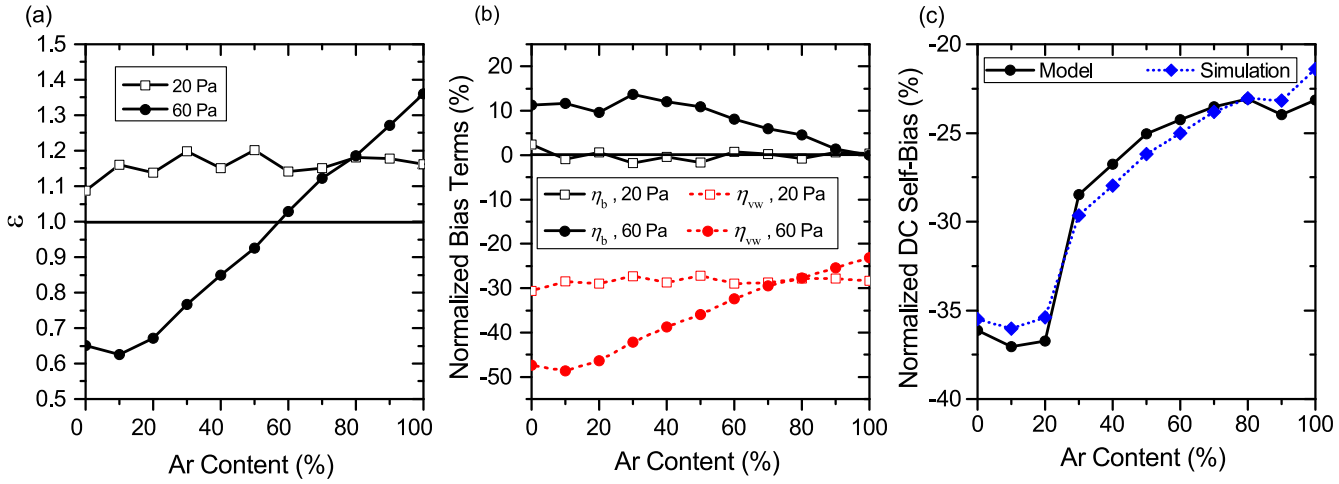

Figure 10. Symmetry parameter ε (a) extracted from the simulation as a function of the argon content in the buffer gas for the 'peaks'-waveform ($N = 3$, $\tilde{\phi}_{tot} = 150$ V) at 20 and 60 Pa. DC self-bias terms, η_{vw} and η_b (b) calculated from the model using simulation data for the 'peaks'-waveform. DC self-bias for the 60 Pa, 'peaks'-waveform ($N = 3$, $\tilde{\phi}_{tot} = 150$ V) from the model and from the simulation (c). The data are normalized by the fixed total voltage amplitude of $\tilde{\phi}_{tot} = 150$ V.

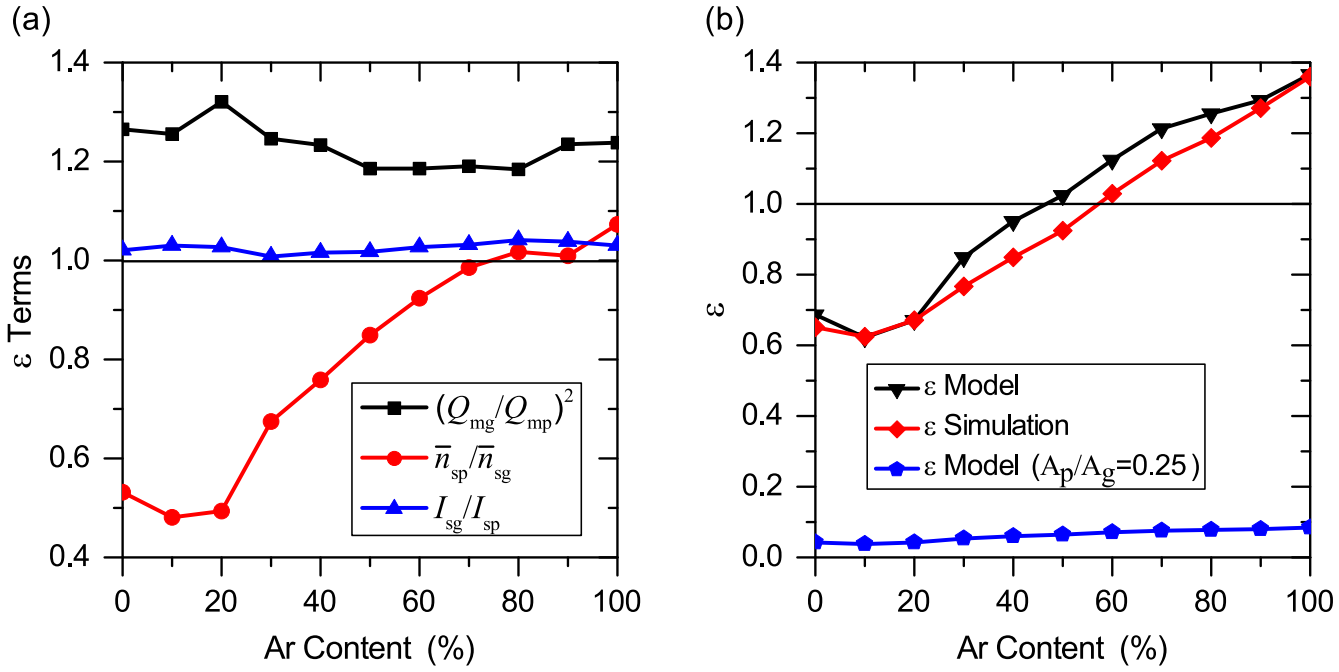

Figure 11. (a) Dependence of the individual ratios in equation (5), including the maximum uncompensated charges in each sheath (Q_{mg}/Q_{mp}), the sheath charged particle densities ($\bar{n}_{sp}/\bar{n}_{sg}$), and the sheath integrals (I_{sg}/I_{sp}) on the argon content in the buffer gas. (b) Variation of the symmetry parameter, ε, with the argon content in the buffer gas as obtained from the model using simulation data as inputs (black triangles), extracted directly from the simulation (red diamonds), and the same model results using an 'artificial' geometric asymmetry factor of $\frac{A_p}{A_g} = 0.25$ (blue pentagons). Both (a) and (b) show results for the 60 Pa, 'peaks'-waveform ($N = 3$, $\tilde{\phi}_{tot} = 150$ V) cases.

The evolution of the total DC self-bias in the experiments at high pressure with increasing argon content (shown in figure 9(b)) is primarily due to the presence of the bulk voltage term η_b, while the η_{vw} term's variation is suppressed by the geometric asymmetry's effect on ε. Therefore, the experimental DC self-bias η evolves due to the interaction of two terms: $\eta_{vw} \approx$ constant, and a counter-acting $\eta_b \to 0$ as the argon content increases to 100%. The two effects together are responsible for the variation of the DC self-bias magnitude in each case in the experiment. This is most easily understood for the single-frequency ($N = 1$) case at 60 Pa (black solid line in figure 9(b)), where the negative DC self-bias generated due to the geometric asymmetry, represented by the 100% argon data point, is countered by the presence of a significant positive bulk voltage term η_b at 0% argon content, where the discharge operates in DA-mode. This results

in a total DC self-bias very near zero for 0% argon content, despite the presence of the geometric asymmetry. As the argon content is increased, η_b decreases in magnitude towards zero, eventually restoring the negative DC self-bias caused by the geometric asymmetry at 100% argon. Similarly, for the 'peaks'-waveform, the negative bias from the driving voltage waveform (η_{vw}) is counter-acted by the presence of a positive η_b at low argon admixtures, which disappears as the Ar/CF_4 gas mixture is changed to pure argon gas. A similar albeit reversed situation is true for the 'valleys'-waveform, where a positive η_{vw} is counter-acted by a negative η_b, whose absolute value decreases to zero at 100% Ar. These effects minimally affect the total DC self-bias η as a function of increasing argon content at the lower pressure, because the electronegativity of the discharge is too low to induce significant DA-mode bulk electric fields and to significantly change the symmetry parameter ε.

At 60 Pa, the dependence of the DC self-bias on the argon content is different for the 'peaks'- and 'valleys'-waveform in the experiment and in the simulation (see figure 9(b)). For the 'peaks'-waveform, the simulated DC self-bias retains a decrease in the magnitude of η_{vw} from ε, leading to the overall decrease in magnitude of the negative DC self-bias, despite the positive η_b decreasing to zero as the argon content approaches 100%. This stands in contrast to the experimental data, where the suppression of changes in η_{vw} allows the overall DC self-bias to increase in magnitude with increasing argon content. An analogous argument is valid for the 'valleys'-waveform. The dependence of this DC self-bias phenomenon on the discharge geometry, i.e. either geometrically asymmetric $\left(\frac{A_p}{A_g} < 1\right)$ or geometrically symmetric $\left(\frac{A_p}{A_g} = 1\right)$, implies that the discharge geometry becomes relevant when using an electronegative gas or admixture.

6. Conclusions

The spatio-temporal electron impact excitation dynamics and the generation of a DC self-bias through VWT were investigated experimentally, with the aid of numerical simulations and subsequent model calculations in an Ar/CF_4 CCP discharge at both 20 and 60 Pa as a function of the mixing ratio between the electronegative CF_4 and electropositive Ar gas components. Triple-frequency 'peaks'- and 'valleys'-waveforms were used to explore the effects of changing the gas composition on the electron power absorption dynamics and the subsequent generation of a DC self-bias. Mode transitions from the DA- to the α-mode across the 0% to 100% argon content interval were observed experimentally for each given waveform and pressure, but the transitions were found to occur at different argon admixtures at different pressures. The mode transition is less pronounced and occurs at smaller argon admixtures at 20 Pa compared to a higher pressure of 60 Pa due to the fact that the electronegativity remains high up to larger argon admixtures at the higher pressure. At 60 Pa an increase of the global electronegativity as a function of the argon admixture was observed for admixtures between 20% and 30%. This counterintuitive finding was explained by the effect of adding small admixtures of electropositive argon to the electronegative CF_4 gas on the spatio-temporal electron dynamics. The numerical simulations qualitatively reproduce the overall trends in the spatio-temporal excitation dynamics and the DC self-bias. Differences in the experimental measurements compared to the numerical simulations and the model calculations are found to be caused by the presence of a geometric discharge asymmetry in the experiment, which is not included in the simulations.

The numerical simulation results provide access to a variety of additional plasma parameters, which could not be measured, such as the spatio-temporal electron attachment rate, the bulk electric field, and the mean electron energy. Based on these insights a detailed fundamental understanding of the spatio-temporal electron dynamics and the mode transitions as a function of the argon admixture to CF_4 was obtained. It was found that the drift electric field in the plasma bulk is reduced substantially as the electronegativity of the discharge is decreased, both as a function of increasing argon content and decreasing pressure. This was identified as the main mechanism that induces a mode transition from the DA- to the α-mode.

Based on this fundamental understanding of the plasma physics and an analytical model, the physical origin of the generation of a DC self-bias as a function of the argon content in the case of 'peaks'- and 'valleys'-waveforms was revealed. The change of the discharge mode induced by increasing the argon content in the buffer gas was found to affect the discharge symmetry and voltage drops across the plasma bulk at a high pressure of 60 Pa. In a geometrically symmetric CCP, this was found to result in a decrease of the magnitude of the DC self-bias as a function of the argon content, while the self-bias remained nearly constant at a lower pressure of 20 Pa, at which the discharge is more electropositive for most argon admixtures. Finally, a geometric discharge asymmetry was found to suppress the variation of the discharge symmetry as a function of the argon content in the buffer gas. This causes the DC self-bias to remain approximately constant as a function of the argon content even at 60 Pa in the experiment.

These findings are expected to be highly valuable for knowledged based plasma process optimization in multi-frequency discharges containing mixtures of electropositive and electronegative gases.

Acknowledgments

Funding from the NSF grant PHY 1601080, by the Deutsche Forschungsgemeinschaft (DFG) via SFB TR 87 (project C1), from the Hungarian National Office for Research, Development, and Innovation (NKFIH) through the grant K-119357, PD-121033, FK-128924, and the J Bolyai Research Fellowship of the HAS (DA) is gratefully acknowledged. This publication is also based upon work supported by the US DOE, Office of Science under contract number DE-SC0012515. This work is part of a dissertation to be

submitted by S Brandt to the Eberly College of Arts and Sciences, West Virginia University, Morgantown, WV, in partial fulfillment of the requirements for the PhD Degree in physics.

ORCID iDs

S Brandt https://orcid.org/0000-0002-8689-4548
B Berger https://orcid.org/0000-0001-7053-2545
Z Donkó https://orcid.org/0000-0003-1369-6150
A Derzsi https://orcid.org/0000-0002-8005-5348
M Koepke https://orcid.org/0000-0001-9631-356X
J Schulze https://orcid.org/0000-0001-7929-5734

References

[1] Rath J 2003 Low temperature polycrystalline silicon: a review on deposition, physical properties and solar cell applications *Sol. Energy Mater. Sol. Cells* **76** 431
[2] Falub C V, Rohrmann H, Bless M, Meduña M, Marioni M, Schneider D, Richter J H and Padrun M 2017 Tailoring the soft magnetic properties of sputtered multilayers by microstructure engineering for high frequency applications *AIP Adv.* **7** 056414
[3] Makabe T and Petrović Z 2006 *Plasma Electronics: Applications in Microelectronic Device Fabrication* (New York: Taylor and Francis)
[4] Donnelly V M and Kornblit A 2013 Plasma etching: yesterday, today, and tomorrow *J. Vac. Sci. Technol.* A **31** 050825
[5] Chu P K, Chen J Y, Wang L P and Huang N 2002 Plasma-surface modification of biomaterials *Mater. Sci. Eng.* R **36** 143
[6] Gomathi N, Sureshkumar A and Neogi S 2008 RF plasma-treated polymers for biomedical applications *Curr. Sci.* **94** 1478
[7] Fridman A and Friedman G 2013 *Plasma Medicine* 1st edn (Oxford UK: Wiley)
[8] Lee H-C, Bang J-Y and Chung C-W 2011 *Thin Solid Films* **519** 7009
[9] Lee H-C, Bang J-Y and Chung C-W 2012 *Appl. Phys. Lett.* **101** 244104
[10] Sobolewski M A and Kim J-H 2007 *J. Appl. Phys.* **102** 113302
[11] Schulze J, Schüngel E and Czarnetzki U 2012 *Appl. Phys. Lett.* **100** 024102
[12] Berger B, Steinberger T, Schüngel E, Koepke M, Mussenbrock T, Awakowicz P and Schulze J 2017 Enhanced power coupling efficiency in inductive discharges with RF substrate bias driven at consecutive harmonics with adjustable phase *Appl. Phys. Lett.* **111** 201601
[13] Schulze J, Schüngel E, Donkó Z and Czarnetzki U 2010 Charge dynamics in capacitively coupled radio frequency discharges *J. Phys. D: Appl. Phys.* **43** 225201
[14] Donkó Z, Schulze J, Czarnetzki U, Derzsi A, Hartmann P, Korolov I and Schüngel E 2012 Fundamental investigations of capacitive radio frequency plasmas: simulations and experiments *Plasma Phys. Control. Fusion* **54** 124003
[15] Schulze J, Gans T, O'Connell D, Czarnetzki U, Ellingboe A R and Turner M M 2007 Space and phase resolved plasma parameters in an industrial dual-frequency capacitively coupled radio-frequency discharge *J. Phys. D: Appl. Phys.* **40** 7008
[16] Waskoenig J and Gans T 2010 Nonlinear frequency coupling in dual radio-frequency driven atmospheric pressure plasmas *Appl. Phys. Lett.* **96** 181501
[17] Gans T, Schulze J, O'Connell D, Czarnetzki U, Faulkner R, Ellingboe A R and Turner M M 2006 Frequency coupling in dual frequency capacitively coupled radio-frequency plasmas *Appl. Phys. Lett.* **89** 261502
[18] Song S-H and Kushner M J 2012 Control of electron energy distributions and plasma characteristics of dual frequency, pulsed capacitively coupled plasmas sustained in Ar and $Ar/CF4/O_2$ *Plasma Sources Sci. Technol.* **21** 055028
[19] Donkó Z, Schulze J, Hartmann P, Korolov I, Czarnetzki U and Schüngel E 2010 The effect of secondary electrons on the separate control of ion energy and flux in dual-frequency capacitively coupled radio frequency discharges *Appl. Phys. Lett.* **97** 081501
[20] Qin X V, Ting Y-H and Wendt A E 2010 Tailored ion energy distributions at an rf-biased plasma electrode *Plasma Sources Sci. Technol.* **19** 065014
[21] Patterson M M, Chu H-Y and Wendt A E 2007 *Plasma Sources Sci. Technol.* **16** 257
[22] Lafleur T 2016 Tailored-waveform excitation of capacitively coupled plasmas and the electrical asymmetry effect *Plasma Sources Sci. Technol.* **25** 013001
[23] Heil B G, Czarnetzki U, Brinkmann R P and Mussenbrock T 2008 On the possibility of making a geometrically symmetric RF-CCP discharge electrically asymmetric *J. Phys. D: Appl. Phys.* **41** 165202
[24] Donkó Z, Schulze J, Heil B G and Czarnetzki U 2009 PIC simulations of the separate control of ion flux and energy in CCRF discharges via the electrical asymmetry effect *J. Phys. D: Appl. Phys.* **42** 025205
[25] Schulze J, Schüngel E and Czarnetzki U 2009 The electrical asymmetry effect in capacitively coupled radio frequency discharges measurements of dc self bias, ion energy and ion flux *J. Phys. D: Appl. Phys.* **42** 092005
[26] Czarnetzki U, Schulze J, Schüngel E and Donkó Z 2011 The electrical asymmetry effect in capacitively coupled radio-frequency discharges *Plasma Sources Sci. Technol.* **20** 024010
[27] Bienholz S, Styrnoll T and Awakowicz P 2014 On the electrical asymmetry effect in large area multiple frequency capacitively coupled plasmas *J. Phys. D: Appl. Phys.* **47** 065201
[28] Schüngel E, Schulze J, Donkó Z and Czarnetzki U 2011 Power absorption in electrically asymmetric dual frequency capacitive radio frequency discharges *Phys. Plasmas* **18** 013503
[29] Schulze J, Schüngel E, Donkó Z and Czarnetzki U 2010 Excitation dynamics in electrically asymmetric capacitively coupled radio frequency discharges: experiment, simulation, and model *Plasma Sources Sci. Technol.* **19** 045028
[30] Schüngel E, Eremin D, Schulze J, Mussenbrock T and Czarnetzki U 2012 The electrical asymmetry effect in geometrically asymmetric capacitive radio frequency plasmas *J. Appl. Phys.* **112** 053302
[31] Schulze J, Schüngel E, Donkó Z and Czarnetzki U 2011 The electrical asymmetry effect in multi-frequency capacitively coupled radio frequency discharges *Plasma Sources Sci. Technol.* **20** 015017
[32] Derzsi A, Korolov I, Schüngel E, Donkó Z and Schulze J 2013 Electron heating and control of ion properties in capacitive discharges driven by customized voltage waveforms *Plasma Sources Sci. Technol.* **22** 065009
[33] Zhang Y, Zafar A, Coumou D, Shannon S and Kushner M 2015 Control of ion energy distribution using phase shifting in multi-frequency capacitively coupled plasmas *J. Appl. Phys.* **117** 233302

[34] Gibson A R, Greb A, Graham W G and Gans T 2015 Tailoring the nonlinear frequency coupling between odd harmonics for the optimization of charged particle dynamics in capacitively coupled oxygen plasmas *Appl. Phys. Lett.* **106** 054102

[35] Bora B 2015 Effect of driving voltages in dual capacitively coupled radio frequency plasma: a study by nonlinear global model *Phys. Plasmas* **22** 103503

[36] Bora B 2015 Studies on the effect of finite geometrical asymmetry in dual capacitively coupled radio frequency plasma *Plasma Sources Sci. Technol.* **24** 054002

[37] Lafleur T, Delattre P A, Johnson E V and Booth J P 2012 Separate control of the ion flux and ion energy in capacitively coupled radio-frequency discharges using voltage waveform tailoring *Appl. Phys. Lett.* **101** 124104

[38] Lafleur T, Delattre P A, Johnson E V and Booth J P 2013 Capacitively coupled radio-frequency plasmas excited by tailored voltage waveforms *Plasma Phys. Control. Fusion* **55** 124002

[39] Coumou D J, Clark D H, Kummerer T, Hopkins M, Sullivan D and Shannon S 2014 Ion energy distribution skew control using phase-locked harmonic RF bias drive *IEEE Trans. Plasma Sci.* **42** 1880

[40] Bruneau B, Lafleur T, Booth J P and Johnson E 2016 Controlling the shape of the ion energy distribution at constant ion flux and constant mean ion energy with tailored voltage waveforms *Plasma Sources Sci. Technol.* **25** 025006

[41] Schüngel E, Donkó Z, Hartmann P, Derzsi A, Korolov I and Schulze J 2015 Customized ion flux-energy distribution functions in capacitively coupled plasmas by voltage waveform tailoring *Plasma Sources Sci. Technol.* **24** 045013

[42] O'Neill C, Waskoenig J and Gans T 2012 Tailoring electron energy distribution functions through energy confinement in dual radio-frequency driven atmospheric pressure plasmas *Appl. Phys. Lett.* **101** 154107

[43] O'Connell D, Gans T, Semmler E and Awakowicz P 2008 The role of the relative voltage and phase for frequency coupling in a dual-frequency capacitively coupled plasma *Appl. Phys. Lett.* **93** 081502

[44] Diomede P, Economou D J, Lafleur T, Booth J P and Longo S 2014 Radio-frequency capacitively coupled plasmas in hydrogen excited by tailored voltage waveforms: comparison of simulations with experiments *Plasma Sources Sci. Technol.* **23** 065049

[45] Schüngel E, Mohr S, Iwashita S, Schulze J and Czarnetzki U 2013 The effect of dust on electron heating and dc self-bias in hydrogen diluted silane discharges *J. Phys. D: Appl. Phys.* **46** 175205

[46] Schulze J, Derzsi A and Donkó Z 2011 Electron heating and the electrical asymmetry effect in dual-frequency capacitive CF_4 discharges *Plasma Sources Sci. Technol.* **20** 045008

[47] Johnson E V, Verbeke T, Vanel J-C and Booth J-P 2010 Nanocrystalline silicon film growth morphology control through RF waveform tailoring *J. Phys. D: Appl. Phys.* **43** 412001

[48] Johnson E V, Delattre P A and Booth J-P 2012 Microcrystalline silicon solar cells deposited using a plasma process excited by tailored voltage waveforms *Appl. Phys. Lett.* **100** 133504

[49] Johnson E V, Pouliquen S, Delattre P A and Booth J-P 2012 Hydrogenated microcrystalline silicon thin films deposited by RF-PECVD under low ion bombardment energy using voltage waveform tailoring *J. Non-Cryst. Solids* **358** 1974

[50] Schüngel E, Hofmann R, Mohr S, Schulze J, Röpcke J and Czarnetzki U 2015 Evaluation of the electrical asymmetry effect by spectroscopic measurements of capacitively coupled discharges and silicon thin film depositions *Thin Solid Films* **574** 60

[51] Schüngel E, Mohr S, Schulze J and Czarnetzki U 2015 Prevention of lateral ion flux inhomogneities in large area capacitive radio frequency plasmas via the electrical asymmetry effect *Appl. Phys. Lett.* **106** 054108

[52] Franek J, Brandt S, Berger B, Liese M, Barthel M, Schüngel E and Schulze J 2015 Power supply and impedance matching to drive technological radio-frequency plasmas with customized voltage waveforms *Rev. Sci. Instrum.* **86** 053504

[53] Schmidt F, Schulze J, Johnson E, Booth J-P, Keil D, French D, Trieschmann J and Mussenbrock T 2018 Multi frequency matching for voltage waveform tailoring *Plasma Sources Sci. Technol.* **27** 095012

[54] Wang J, Dine S, Booth J-P and Johnson E V 2019 Experimental demonstration of multifrequency impedance matching for tailored voltage waveform plasmas *J. Vac. Sci. Technol.* A **37** 021303

[55] Schüngel E, Brandt S, Korolov I, Derzsi A, Donkó Z and Schulze J 2015 On the self-excitation mechanisms of plasma series resonance oscillations in single- and multi-frequency capacitive discharges *Phys. Plasmas* **22** 043512

[56] Brandt S *et al* 2016 Electron power absorption dynamics in capacitive radio frequency discharges driven by tailored voltage waveforms in CF_4 *Plasma Sources Sci. Technol.* **25** 045015

[57] Donkó Z *et al* 2017 Experimental benchmark of kinetic simulations of capacitively coupled plasmas in molecular gases *Plasma Phys. Control. Fusion* **60** 014010

[58] Xi-Feng W, Jia W-Z, Song Y-H, Zhang Y-Y, Dai Z-L and Wang Y-N 2017 Hybrid simulation of electron energy distributions and plasma characteristics in pulsed RF CCP sustained in Ar and SiH_4/Ar discharges *Phys. Plasmas* **24** 113503

[59] Proshina O V, Rakhimova T V, Lopaev D V, Šamara V, Baklanov M R and de Marneffe J-F 2015 Experimental and theoretical study of RF capacitively coupled plasmas in Ar-CF_4-CF_3I mixtures *Plasma Sources Sci. Technol.* **24** 055006

[60] Fischer G, Ouaras K, Drahi E, Bruneau B and Johnson E V 2018 Excitation of Ar, O_2, and SF_6/O_2 plasma discharges using tailored voltage waveforms: control of surface ion bombardment energy and determination of the dominant electron excitation mode *Plasma Sources Sci. Technol.* **27** 074003

[61] Bruneau B, Novikova T, Lafleur T, Booth J P and Johnson E V 2015 Control and optimization of the slope asymmetry effect in tailored voltage waveforms for capacitively coupled plasmas *Plasma Sources Sci. Technol.* **24** 015021

[62] Bruneau B, Novikova T, Lafleur T, Booth J P and Johnson E V 2014 Ion flux asymmetry in radiofrequency capacitively-coupled plasmas excited by sawtooth-like waveforms *Plasma Sources Sci. Technol.* **23** 065010

[63] Bruneau B, Gans T, O'Connell D, Greb A, Johnson E V and Booth J P 2015 Strong ionization asymmetry in a geometrically symmetric radio frequency capacitively coupled plasma induced by sawtooth voltage waveforms *Phys. Rev. Lett.* **114** 125002

[64] Bruneau B *et al* 2016 Effect of gas properties on the dynamics of the electrical slope asymmetry effect in capacitive plasmas: comparison of Ar, H_2 and CF_4 *Plasma Sources Sci. Technol.* **25** 01LT02

[65] Belenguer P and Boeuf J P 1990 Transition between different regimes of rf glow discharges *Phys. Rev.* A **41** 4447

[66] Schulze J, Donkó Z, Luggenhölscher D and Czarnetzki U 2009 Different modes of electron heating in dual-frequency capacitively coupled radio frequency discharges *Plasma Sources Sci. Technol.* **18** 034011

[67] Schulze J, Heil B G, Luggenhölscher D, Brinkmann R P and Czarnetzki U 2008 Stochastic heating in asymmetric capacitively coupled RF discharges *J. Phys. D: Appl. Phys.* **41** 195212

[68] Gozadinos G, Turner M M and Vender D 2001 Collisionless electron heating by capacitive rf sheaths *Phys. Rev. Lett.* **87** 135004

[69] Tatanova M, Golubovskii Y B, Smirnov A S, Seimer G, Basner R and Kersten H 2009 Electron stochastic heating in a capacitively coupled low-pressure argon rf-discharge *Plasma Sources Sci. Technol.* **18** 025026

[70] Heil B G, Schulze J, Mussenbrock T, Brinkmann R P and Czarnetzki U 2008 Numerical modeling of electron beams accelerated by the radio frequency boundary sheath *IEEE Trans. Plasma Sci.* **36** 1404

[71] Schulze J, Derzsi A, Dittmann K, Hemke T, Meichnser J and Donkó Z 2011 Ionization by drift and ambipolar electric fields in electronegative capacitive radio frequency plasmas *Phys. Rev. Lett.* **107** 275001

[72] Küllig C, Dittmann K, Wegner T, Sheykin I, Matyash K, Loffhagen D, Schneider R and Meichsner J 2012 Dynamics and electronegativity of oxygen rf plasmas *Contrib. Plasma Phys.* **52** 836

[73] Liu G-H, Liu Y-X, Wen D-Q and Wang Y-N 2015 Heating mode transition in capacitively coupled CF_4 discharges: comparison of experiments with simulations *Plasma Sources Sci. Technol.* **24** 034006

[74] Dittmann K, Matyash K, Nemschokmichal S, Meichsner J and Schneider R 2010 Excitation mechanisms and sheath dynamics in capacitively coupled radio-frequency oxygen plasmas *Contrib. Plasma Phys.* **50** 942

[75] Killer C, Bandelow G, Matyash K, Schneider R and Melzer A 2013 Observation of X mode electron heating in dusty argon radio frequency discharges *Phys. Plasmas* **20** 083704

[76] Tochikubo F, Makabe T, Kakuta S and Suzuki A 1992 Study of the structure of radio-frequency glow-discharges in CH_4 and H_2 by spatiotemporal optical-emission spectroscopy *J. Appl. Phys.* **71** 2143

[77] Zhang Z L *et al* 2018 Ionization asymmetry effects on the properties modulation of atmospheric pressure dielectric barrier discharge sustained by tailored voltage waveforms *Phys. Plasmas* **25** 043502

[78] Gibson A *et al* 2019 Disrupting the spatio-temporal symmetry of the electron dynamics in atmospheric pressure plasmas by voltage waveform tailoring *Plasma Sources Sci. Technol.* **28** 01LT01

[79] Johnson E V, Delattre P A and Booth J-P 2012 Microcrystalline silicon solar cells deposited using a plasma process excited by tailored voltage waveforms *Appl. Phys. Lett.* **100** 133504

[80] Johnson E V, Pouliquen S, Delattre P A and Booth J-P 2012 Hydrogenated microcrystalline silicon thin films deposited by RF-PECVD under low ion bombardment energy using voltage waveform tailoring *J. Non-Cryst. Solids* **358** 1974

[81] Bruneau B, Lepecq M, Wang J, Dornstetter J-C, Maurice J-L and Johnson E-V 2014 Effect of ion energy on microcrystalline silicon material and devices: a study using tailored voltage waveforms *IEEE J. Photovolt.* **4** 1354

[82] Hrunski D *et al* 2013 Deposition of microcrystalline intrinsic silicon by the Electrical Asymmetry Effect technique *Vacuum* **87** 114–8

[83] Hrunski D, Janssen A, Fritz T, Hegemann T, Clark C, Schreiber U and Grabosch G 2013 The influence of the electrical asymmetry effect on deposition uniformity of thin silicon film *Thin Solid Films* **532** 56–9

[84] Tochikubo F, Suzuki A, Kakuta S, Terazono Y and Makabe T 1990 Study of the structure in rf glow discharges in SiH_4/H_2 by spatiotemporal optical emission spectroscopy: influence of negative ions *J. Appl. Phys.* **68** 5532

[85] Zhang Q-Z, Wang Y-N and Bogaerts A 2014 Heating mode transition in a hybrid direct current/dual-frequency capacitively coupled CF_4 discharge *J. Appl. Phys.* **115** 223302

[86] Hemke T, Eremin D, Mussenbrock T, Derzsi A, Donkó Z, Dittmann K, Meichsner J and Schulze J 2013 Ionization by bulk heating of electrons in capacitive radio frequency atmospheric pressure microplasmas *Plasma Sources Sci. Technol.* **22** 015012

[87] Gans T, O'Connell D, Schulz-von der Gathen V and Waskoenig J 2010 The challenge of revealing and tailoring the dynamics of radio-frequency plasmas *Plasma Sources Sci. Technol.* **19** 034010

[88] Mahony C M O, Wazzan R A and Graham W G 1997 Sheath dynamics observed in a 13.56 MHz-driven plasma *Appl. Phys. Lett.* **71** 608

[89] Schulze J, Donkó Z, Heil B G, Luggenhölscher D, Mussenbrock T, Brinkmann R P and Czarnetzki U 2008 Electric field reversals in the sheath region of capacitively coupled radio frequency discharges at different pressures *J. Phys. D: Appl. Phys.* **41** 105214

[90] Czarnetzki U, Luggenhölscher D and Döbele H F 1999 Space and time resolved electric field measurements in helium and hydrogen RF-discharges *Plasma Sources Sci. Technol.* **8** 230

[91] Lieberman M A and Godyak V A 1998 From Fermi acceleration to collisionless discharge heating *IEEE Trans. Plasma Sci.* **26** 955

[92] Surendra M and Graves D B 1991 Electron acoustic waves in capacitively coupled, low-pressure rf glow discharges *Phys. Rev. Lett.* **66** 1469

[93] Salabas A, Marques L, Jolly J and Alves L L 2004 Systematic characterization of low-pressure capacitively coupled hydrogen discharges *J. Appl. Phys.* **95** 4605

[94] Vender D and Boswell R W 1990 Numerical modeling of low-pressure RF plasmas *IEEE Trans. Plasma Sci.* **18** 725

[95] Lafleur T, Chabert P and Booth J P 2014 Electron heating in capacitively coupled plasmas revisited *Plasma Sources Sci. Technol.* **23** 035010

[96] Schulze J, Schüngel E, Derzsi A, Korolov I, Mussenbrock T and Donkó Z 2014 Complex electron heating in capacitive multi-frequency plasmas *IEEE Trans. Plasma Sci.* **42** 2780

[97] Schulze J, Donkó Z, Derzsi A, Korolov I and Schüngel E 2015 The effect of ambipolar electric fields on the electron heating in capacitive RF plasmas *Plasma Sources Sci. Technol.* **24** 015019

[98] Proto A and Gudmundsson J T 2018 The influence of secondary electron emission and electron reflection on a capacitively coupled oxygen discharge *Atoms* **6** 65

[99] Proto A and Gudmundsson J T 2018 The role of surface quenching of the singlet delta molecule in a capacitively coupled oxygen discharge *Plasma Sources Sci. Technol.* **27** 074002

[100] Toneli D A, Pessoa R S, Roberto M and Gudmundsson J T 2019 A global model study of low pressure high density CF_4 discharge *Plasma Sources Sci. Technol.* **28** 025007

[101] Liu G H, Liu Y-X, Bai L-S, Zhao K and Wang Y-N 2018 Experimental investigation of mode transitions in asymmetric capacitively coupled radio-frequency Ne and CF_4 plasmas *Phys. Plasmas* **25** 023515

[102] Liang Y-S, Liu G-H, Xue C, Liu Y-X and Wang Y-N 2017 Fluid simulation of species concentrations in capacitively coupled N_2/Ar plasmas: effect of gas proportion *J. Appl. Phys.* **121** 203302

[103] Proshina O V, Rakhimova T V, Rakhimov A T and Voloshin D G 2010 Two modes of capacitively coupled rf discharge in CF_4 *Plasma Sources Sci. Technol.* **19** 065013

[104] Schulze J, Schuengel E, Donkó Z, Luggenhoelscher D and Czarnetzki U 2010 Phase resolved optical emission spectroscopy: a non-intrusive diagnostic to study electron dynamics in capacitive radio frequency discharges *J. Phys. D: Appl. Phys.* **43** 124016

[105] Böhm C and Perrin J 1991 Spatially resolved optical emission and electrical properties of SiH_4 RF discharges at 13.56 MHz in a symmetric parallel-plate configuration *J. Phys. D: Appl. Phys.* **24** 865

[106] Greb A, Gibson A R, Niemi K, O'Connell D and Gans T 2015 Influence of surface conditions on plasma dynamics and electron heating in a radio-frequency driven capacitively coupled oxygen plasma *Plasma Sources Sci. Technol.* **24** 044003

[107] Mahony C M O, Al Wazzan R and Graham W G 1997 Sheath dynamics observed in a 13.56 MHz-driven plasma *Appl. Phys. Lett.* **71** 608

[108] Wise L W, Smith M W, Glennon B M, Lidén K and (NIST ASD Team) 2014 *NIST Atomic Spectra Database* (ver.5.6.1) (Gaithersburg, MD: National Institute of Standards and Technology) (https://doi.org/10.1103/PhysRevA.60.947)

[109] Birdsall C K 1991 Particle-in-cell charged-particle simulations, plus Monte Carlo collisions with neutral atoms, PIC-MCC *IEEE Trans. Plasma Science* **19** 65

[110] Verboncoeur J P 2005 Particle simulation of plasmas: review and advances *Plasma Phys. Control. Fusion* **47** A231

[111] Matyash K, Schneider R, Taccogna F, Hatayama A, Longo S, Capitelli M, Tskhakaya D and Bronold F X 2007 Particle in cell simulation of low temperature laboratory plasmas *Contrib. Plasma Phys.* **47** 595

[112] Donkó Z and Petrović Z L 2007 Ion behavior in capacitively-coupled dual-frequency discharges *J. Phys.: Conf. Ser.* **86** 12011

[113] Georgieva V, Bogaerts A and Gijbels R 2003 Numerical study of $Ar/CF_4/N_2$ discharges in single- and dual-frequency capacitively coupled plasma reactors *J. Appl. Phys.* **93** 2369

[114] Kurihara M, Petrović Z L and Makabe T 2000 Transport coefficients and scattering cross-sections for plasma modelling in CF_4-Ar mixtures: a swarm analysis *J. Phys. D: Appl. Phys.* **33** 2146

[115] Bonham R A 1994 Electron impact cross section data for carbon tetraflouride *Japan. J. Appl. Phys.* **33** 4157

[116] Phelps A V and Petrovic Z L 1999 *Plasma Sources Sci. Technol.* **8** R21

[117] Phelps A V 1994 *J. Appl. Phys.* **76** 747

[118] Georgieva V, Bogaerts A and Gijbels R 2004 *J. Appl. Phys.* **94** 3748

[119] Georgieva V, Bogaerts A and Gijbels R 2004 Numerical investigation of ion-energy-distribution functions in single and dual frequency capacitively coupled plasma reactors *Phys. Rev.* E **69** 026406

[120] Georgieva V, Bogaerts A and Gijbels R 2003 Numerical study of $Ar/CF_4/N_2$ discharges in single- and dual-frequency capacitively coupled plasma reactors *J. Appl. Phys.* **94** 3748

[121] Rauf S and Kushner M J 1997 Argon metastable densities in radio frequency Ar, Ar/O_2, and Ar/CF_4 electrical discharges *J. Appl. Phys.* **82** 2805

[122] Denpoh K and Nanbu K 2000 Self-consistent particle simulation of radio frequency CF_4 discharge: effect of gas pressure *Japan. J. Appl. Phys.* **39** 2804

[123] Kollath R 1956 *Encyclopedia of Physics* vol 21 ed S Flügge (Berlin: Springer)

[124] Czarnetzki U, Heil B G, Schulze J, Donkó Z, Mussenbrock T and Brinkmann R P 2009 The electrical asymmetry effect—a novel and simple method for separate control of ion energy and flux in capacitively coupled RF discharges *J. Phys.: Conf. Ser.* **162** 012010

[125] Boeuf J P and Belenguer P 1992 Transition from a capacitive to a resistive regime in a silane radio frequency discharge and its possible relation to powder formation *J. Appl. Phys.* **71** 4751

[126] Schüngel E, Korolov I, Bruneau B, Derzsi A, Johnson E, O'Connell D, Gans T, Booth J-P, Donkó Z and Schulze J 2016 Tailored voltage waveform capacitively coupled plasmas in electronegative gases: frequency dependence of asymmetry effects *J. Phys. D: Appl. Phys.* **49** 265203

[127] Brinkmann R P 2011 *J. Phys. D: Appl. Phys.* **44** 042002